DESIGN & ANALYSIS OF DUAL PEAK-DOUBLE PLASMONIC LAYERED PCF SENSORS

by

Safin Zaman (180021119)

Ali Ahnaf Hassan (180021322)

Muhammad Alif Al Hosain (180021324)

A Thesis Submitted to the Academic Faculty in Partial Fulfillment of the Requirements for the Degree of

BACHELOR OF SCIENCE IN ELECTRICAL AND ELECTRONIC ENGINEERING

Department of Electrical and Electronic Engineering

Islamic University of Technology (IUT)

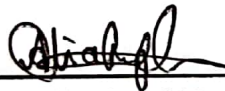Gazipur, Bangladesh

May 2023

I

DECLARATION

We, the authors of this report entitled " DESIGN & ANALYSIS OF DUAL PEAK-DOUBLE PLASMONIC LAYERED PCF SENSORS ", hereby declare that this report and all the findings presented in it are our own.

Submitted by:

_____

Safin Zaman

Student ID: 180021119

_____

Ali Ahnaf Hassan

Student ID: 180021322

_____

Muhammad Alif Al Hosain

Student ID: 180021324

_____

DESIGN & ANALYSIS OF DUAL PEAK-DOUBLE PLASMONIC LAYERED PCF SENSORS

Approved by:

Prof. Dr. Mohammad Rakibul Islam

Supervisor and Head

Department of Electrical and Electronic Engineering

Islamic University of Technology (IUT)

Boardbazar, Gazipur-1704.

Date: 28-05-23

ACKNOWLEDGEMENT

"All praise and gratitude be to Allah, the Most Beneficent, the Most Merciful."

By the grace of our almighty Allah (SWT), we were able to complete our thesis and achieve subsequent results.

We would like to extend our sincerest gratitude to our thesis supervisor, Professor Md. Rakibul Islam from the Department of Electrical and Electronic Engineering at the Islamic University of Technology, for his unwavering support and guidance. We couldn't have asked for a better mentor to guide us on this journey. His helpful demeanor, patience and continuous motivation are what helped us to carry on with our thesis work. We would also like to thank all of the distinguished faculty members in the department of Electrical and Electronic Engineering. Our research has been significantly influenced by their insightful recommendations, criticism, and advice.

Lastly, we can proudly say that today, we are in this position due to the several sacrifices made by our lovely parents, motivation and direction from our seniors and friends. Their constant support and motivation are the reason for our success and we are utterly grateful for that.

ABSTRACT

A number of researchers have established themselves in the area of PCF-based SPR sensors with innovative designs achieving exceptional sensing performance. The majority of designs, however, either show low sensitivity with greater loss or show high sensitivity with the disadvantage of higher confinement loss, which makes designing challenging. The designs may also get complex in order to attain high sensitivities, which is the most essential factor. In our thesis, we employ a novel plasmonic material configuration in which Silver (Ag) and Ga-doped ZnO (GZO) work together to detect analytes. The sensor's detecting capabilities are improved by the presence of two peaks within the same Refractive Index (RI). The first peak is caused by GZO, and the second peak is caused by Ag. In terms of y-polarization, a DPSS of 27,341.5 nm/RIU is found which is the highest number reported to date. The amplitude sensitivity (AS) of the sensor is 875.72 RIU^{-1}, and the wavelength sensitivity (WS) is 27,360 nm/RIU. The sensor also exhibits a high amplitude resolution of 1.496×10^{-5} and a wavelength resolution of 6.032×10^{-6}. A linearity of $R^2=0.9973$ and a FOM of 243.4 RIU^{-1} can be seen from the sensor. After conducting a thorough fabrication tolerance analysis, we find that both the confinement loss and the resonant wavelength shift are unaffected by a ±10-tolerance limit. A wide range of RI up to 1.27 to 1.41 is investigated, which broadens its potential applicability to the detection of pharmaceuticals and other compounds. In addition, the sensing parameters in RIs that were not numerically analyzed have been sought through the use of machine learning regression techniques in this study. No relevant work was found which used regression algorithms to analyze the performance parameters were found to the best of our knowledge. As input, the RI of the analyte is given to the algorithm while the output target variables are the shift in the GZO and Ag peak resonant wavelengths in two consecutive RIs respectively. The accuracy of the Random Forest Regressor was determined to be 90.176%, whereas that of the K-Nearest Neighbors Regressor was 95.54%. This research presents a new approach to assessing sensor performance metrics, which not only facilitates quicker and more accurate predictions but also saves considerable amounts of time.

Table of Contents

List of Tables

List of Figures

List of Acronyms

SPR`	Surface Plasmon Resonance
SPW	Surface Plasmon Wave
PCF	Photonic Crystal Fiber
AS	Amplitude Sensitivity
WS	Wavelength Sensitivity
DPSS	Double Peak Shift Sensitivity
TIR	Total Internal Reflection
PMMA	Poly (methyl Methacrylate)
TOPAS	Tapered Optical Fiber Polymer Cladding Sensor
HDPE	High-Density Polyethylene
IG-PCF	Index Guiding Photonic Crystal Fiber
PBG-PCF	Photonic Bandgap Photonic Crystal Fiber
M-TIR	Modified Total Internal Reflection
UV	Ultraviolet
SPP	Surface Plasmon Polariton
LSPR	Localized Surface Plasmon Resonance
RIU	Refractive Index Unit
PQF	Photonic Quasi-Crystal Fiber
RI	Refractive Index
AZO	Aluminum-doped Zinc Oxide
NIR	Near-Infrared Range
GZO	Gallium-doped Zinc Oxide
CL	Confinement Loss
ITO	Indium Tin Oxide
LOD	Limit of Detection
FOM	Figure of Merit
FWHM	Full Width at Half Maximum
ML	Machine Learning

ANN	Artificial Neural Network
GAN	Genetic Adversarial Networks
RFR	Random Forrest Regressor
LR	Logistic Regressor
K-NR	K-Nearest Neighbors Regressor
CVD	Chemical Vapor Deposition
ALD	Atomic Layer Deposition
FEM	Finite Element Method
PML	Perfectly Matched Layer

CHAPTER – 1

INTRODUCTION

1.1 Background:

Surface plasmon resonance (SPR) is a phenomenon which occurs at the interface of a metal layer and a dielectric medium [1]. Surface plasmon waves (SPWs), which are collective oscillations of free electrons associated with the incident light, are generated when polarized light interacts with this metal-dielectric junction [2]. This coupling results in a significant change in the reflected power, known as surface plasmon resonance. It is a dynamic sensing technology with numerous potential applications. SPR allows for the label-free detection of biomolecular interactions in biomedical research and diagnostics, including protein-protein interactions [3], antibody-antigen binding [4], and DNA hybridization [5], as well as the real-time tracking of binding kinetics and sensitivities [6]. SPR provides quick and sensitive detection of pollutants and analytes and is utilized in environmental monitoring [7], food safety analysis, and quality control [8]–[16]. SPR has also been used in surface characterization [17], biosensing technologies [18]–[29], and material research [30]–[32], advancing numerous disciplines. SPR technologies keep advancing innovation and making contributions to numerous fields thanks to its capacity to provide real-time, label-free, and sensitive detection.

Incorporating photonic crystal fibers (PCF) is one promising approach to SPR sensing technology. PCF is an advanced form of optical fiber with a particular microstructure which includes a regular pattern of air holes running along its length [33], [34]. Also, single-mode operation and effective confinement of the light within the fiber core is ensured by the microstructure of PCF, which gives precise control over light propagation. This distinctive design has many benefits for SPR sensing applications. Such as, this makes it feasible for the guided light to interact with the environment more effectively, thereby improving sensing capabilities [35]. Additionally, PCF offers flexibility in building sensors with customizable sensitivity and response by allowing the manipulation of parameters like pitch, ring number, and air hole size [36].

The origins of surface plasmon resonance (SPR) sensors can be traced back to the early 1970s when Otto and Kretschmann made significant discoveries in the field [37]. These early findings laid the groundwork for the development of SPR-based sensing technologies. In the late 1980s, the Biacore system, the first commercial SPR sensor, was introduced, revolutionizing biosensing with its ability to detect biomolecular rapid interaction without requiring any form of lables [38]. The Biacore system utilized a prism-based configuration, but it faced challenges due to its bulky size and limited miniaturization capabilities. To address these limitations, researchers turned to fiber-based sensors as an alternative. Fiber-based sensors offer unique advantages such as nonlinearity [39], single-mode behavior [40], label-free detection [41], and portability. Among these fiber-based sensors, photonic crystal fiber (PCF)-based SPR sensors have gained significant attention. PCF-based sensors exhibit higher sensitivity and lower resonance peaks compared to other fiber-based sensors, resulting in improved accuracy for detecting unknown analytes.

1.2 Problem Statement:

The development of surface plasmon resonance (SPR) sensors have generated considerable attention due to their adaptability for a wide range of sensing applications. However, multiple challenges and limits in existing SPR-based optical sensors have been found, demanding more exploration and development.

The complexity associated with the fabrication of these sensors is one of the key challenges [42]. The sensor structure is complex and difficult to fabricate due to the selective coating of metal layers and the entry of liquid into the air-hole surface. The fabrication process's need for exact control and alignment could make the production time-consuming and expensive.

Another disadvantage of SPR sensors is their low evanescent field and severe confinement loss. The evanescent field is critical for identifying analyte interactions, and a weak field can result in decreased sensitivity and accuracy. The significant confinement loss has an effect on light propagation, potentially resulting in reduced signal strength and decreased sensor effectiveness. Furthermore, the cost of the internal sensing approach is a challenge. Internal metal-coated PCF sensors require fiber emptying and refilling, making the process time-consuming and labor-

intensive. The delicate nature of the internally coated layer complicates the production process and demands additional processes and maintenance to ensure proper operation [43].

The selection of plasmonic materials becomes crucial in the case of externally metal-coated PCF sensors. Plasmonic materials such as gold, silver, and aluminum are widely used [44]. However, their oxidation susceptibility in aquatic settings might result in a loss in sensing accuracy. To address oxidation-related concerns, more durable and resilient plasmonic materials or surface coatings must be developed [45].

The location and size of air holes in the sensor design might have a substantial impact on manufacturing complexity and cost as well. In SPR sensor research, achieving the desired sensor performance while controlling the complexity and expense of fabrication remains a challenge.

It is essential to address these obstacles and constraints in order to advance SPR sensor technology. Simplifying the fabrication process, improving sensitivity through improved evanescent field characteristics, and reducing overall cost are primary goals for researchers to focus on in order to unlock the full potential of SPR sensors in various sensing applications.

1.3 Research Objectives:

Due to conventional PCF studies growing outdated and saturated, our research focuses on investigating the new technique of SPR-based PCF sensors. The primary goal is to examine alternative SPR sensor designs and how geometric features influence their characteristics. This study modelled our own sensor with ideal performance parameters and investigated potential applications. Here are the key objectives of our research:

1. To determine how the range of wavelengths is affected by the refractive index by measuring amplitude sensitivity (AS) and wavelength sensitivity (WS).
2. Design a structure that follows the external sensing approach.
3. Conducting an in-depth investigation of previous works on SPR-PCF sensors and their limits and work on the improvements.
4. Exploring various combinations of plasmonic materials.
5. Improving the double peak shift sensitivity (DPSS) of a sensor associated with two plasmonic materials.

6. Investigation of the performance and graphical results caused by slight modifications for different parameters.

7. Propose a design which is fabrication friendly.

1.4 Motivation Behind the Research:

Surface Plasmon Resonance (SPR) has gained recognition as a strong method for label-free sensing in multiple fields, including biomedical diagnostics, environmental monitoring, and food safety [46]. SPR sensors are essential instruments for both scientific study and real-world applications because of their excellent sensitivity and specificity in detecting and analyzing bio-molecular interactions.

It is an intriguing opportunity to investigate the possibilities of SPR-based PCF sensors and address the issues that exist in this area. It is possible to create novel SPR sensors with greater performance, increased sensitivity, and a wider range of applications by utilizing PCFs' benefits and combining them with plasmonic materials.

The creation of sophisticated SPR-based PCF sensors is required by an increasing need for sensitive and trustworthy sensing methods. These sensors offer real-time, label-free detection of biomolecules and analytes, which has the potential to change healthcare, environmental monitoring, and food safety. We aim to improve SPR-based PCF sensors and their applications by examining various designs, enhancing sensor characteristics, and discovering novel plasmonic materials.

Furthermore, the motivation behind this research lies in the need to overcome the limitations of traditional SPR sensors and offer innovative solutions that can be fabricated easily, are cost-effective, and provide accurate results. By conducting a comprehensive study on SPR-based PCF sensors, the gap between fundamental research and practical applications can be shortened, ultimately paving the way for the development of next-generation biosensors.

1.5 Thesis Framework:

This thesis book is consisted of 9 chapters. An overview of them are given below.

Chapter 2 describes the structural analysis of PCF sensors and its categories. It also explains the benefits of PCF over traditional optical fibers.

Chapter 3 explains SPR, SPW, LSPR and related terminologies along with their applications and working principles. This chapter also describes how LSPR is advantageous over SPR and the scope of future work in this field.

Chapter 4 contains the analysis of SPR and LSPR based PCF sensors. It gives an outline of evolution of SPR sensors from Prism-based sensors to internal sensing, external sensing and its various types.

Chapter 5 discusses about the widely chosen plasmonic materials along with their background studies. It also explains the factors that need to be considered before choosing a plasmonic material.

Chapter 6 presents the fundamental optimization and analysis terminology and formulas. Important equations used in design, such as the Sellmeier equation, Drude-Lorentz model for Ag, GZO. It portrays the necessary formulas for computing CL, AS, WS, DPSS, FWHM, FOM and sensor length.

Chapter 7 represents our unique work consisting of a dual plasmonic layered sensor based on combination of silver and GZO. The sensor withholds highest recorded value of DPSS till date along with excellent spectral sensitivity and ease of fabrication with a tolerance analysis. We also proposed a use of regression algorithms to predict the sensitivity of the sensor of untested refractive indices which will help to save a lot of time and effort.

Chapter 8 demonstrates how the sensor can be fabricated and the methods that are within reach for making it real. The Stack Method and the Draw Method and the Chemical Vapor Deposition (CVD) techniques are explained along with the experimental setup.

Chapter 9 concludes our book with conclusion along with the future aim and improvements.

CHAPTER – 2

PHOTONIC CRYSTAL FIBERS: AN OVERVIEW

2.1 Introduction:

Photonic Crystal Fibers (PCF) are a special type of optical fibers which are micro-structured whose core and cladding integrate a periodic arrangement of air holes or other dielectric materials. Owing to its distinct optical properties, photonic crystal fibers have attracted the interest of researchers worldwide. The idea of the formation of photonic crystal fibers originated from the efforts of confining light within optical fibers in more novel and effective ways. In 1987, Eli Yablonovitch and Sajeev John independently proposed a photonic bandgap—a frequency range in which electromagnetic waves cannot propagate in a periodic dielectric structure. This inspired the creation of structures that could regulate light propagation like semiconductor bandgaps that control electron flow. Philip Russell and his team at the University of Bath in the United Kingdom were the first to create a photonic crystal lattice within the fiber by strategically placing air holes at regular intervals along the fiber's length. From then, PCF have found its way into a wide array of applications like biosensors, non-linear devices, communication in THz frequency, fiber lasers, etc. for the reason that it can contain light in hollow cores and other geometries that are challenging to produce with regular optical fiber.

2.2 Structural Analysis of PCF:

The central region of the PCF that contains and guides the light is called the core. It usually comprises of a periodic distribution of air holes or other dielectric materials. Surrounding the core is the cladding which has a lower refractive index than that of the core to ensure that light is confined to the core due to the phenomenon of total internal reflection (TIR). Silica is typically used as the background material [47]. However, there are instances of the use of Teflon [48], PMMA [49], TOPAS [50]–[53], Zeonex [54]–[57] and HDPE [58] in place of silica. The air holes in the cladding are responsible for giving PCFs their distinctive optical features such photonic bandgaps, dispersion characteristics, and waveguide modes. The way in which the air holes are arranged determines the structure of the PCF. There are examples of PCF structures in a variety of

geometry, including circles [59], squares [10], hexagons [19], [35], octagons [60]–[62], spirals [63], [64], and hybrids [65].

Core radius, ring count, air hole diameter, and pitch (distance between air holes) are all customizable features of PCFs. Due to the interdependence between the RI and the guiding qualities of optical fibers, the RI of PCFs can be modified to improve their applicability [60].
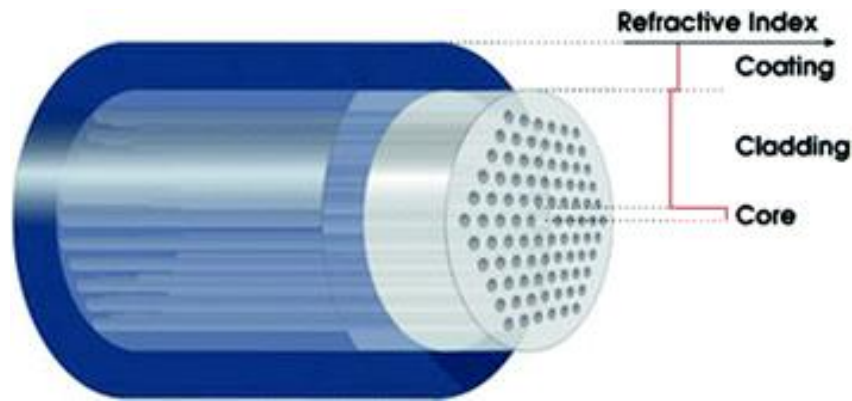
Figure 2.1: Cross-sectional view of a PCF

2.2.1 Categorization of Photonic Crystal Fibers:

Based on guiding mechanism of light, PCF can be classified into two types:

- **Index-Guiding PCF (IG-PCF):** The IG-PCFs restrict and direct light using the disparity in refractive index between the core and cladding. By strategically placing air holes or other elements in the cladding at regular intervals, we may increase the mode confinement inside the core.. Large mode areas, dispersion control, and birefringence are just a few of the distinctive qualities that index-guiding PCFs may display, making them useful in a wide range of applications, from high-power lasers to sensing.

- **Photonic Bandgap PCF (PBG-PCF):** Light confinement and guidance in PBG-PCFs is possible because of the bandgap's photonic nature. Bandgaps are formed in optical fibers by the periodic arrangement of air holes or high-index inclusions inside the cladding, which block the transmission of specific wavelengths. Single-mode guidance and high-power transmission are only two examples of the specialized waveguiding qualities and applications made possible by PBG PCFs' full or partial bandgaps.

Based on the core design, PCFs can be divided into two types:

- **Solid Core Fibers:** Solid-core fibers have a solid core and a cladding, guiding light through a combination of index-guiding and total internal reflection. Larger mode regions allow for increased power management and tunable dispersion characteristics. They are advantageous in the fields of telecommunication and fiber lasers but faces drawbacks like higher losses compared to other PCF structures.

- **Hollow Core Fibers:** This type of PCF contains a core filled with air or other gases instead of a solid material. Since there is no solid substance in the center, hollow core fibers may transmit light with minimal loss all the way from the ultraviolet to the infrared. Compared to solid-core fibers, the air or gas-filled core allows for lower nonlinear effects and higher power handling capacities. Applications for hollow core fibers range from delivering laser beams and high-power pulses to gas sensing and time-resolved spectroscopy.
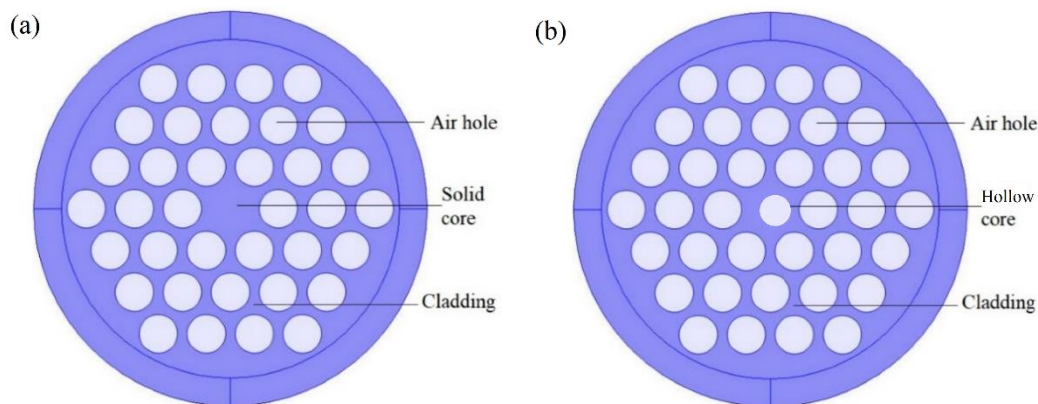
Figure 2.2: (a) Solid Core Fiber and (b) Hollow Core Fiber

2.2.2 Light Guiding Mechanism:

Due to the core's higher refractive index compared to the cladding, typical optical fibers allow light to travel only within the core via total internal reflection. However, depending on the structure, photonic crystal fiber (PCF) exhibits two distinct light guiding methods.

In solid PCFs, a modified form of total internal reflection similar to that utilized in standard fibers is employed. In this case, utilizing silica solid for the core allows for a higher refractive index than

the cladding. The refractive index of the core is lowered by a network of air capillaries in the cladding that surrounds it. These fibers use a technique called modified total internal reflection (M-TIR) to steer the light in the desired direction.

However, the photonic band gap technique is utilized in hollow core fibers. The core of this guiding mechanism has air holes in it, causing its refractive index to be lower than that of the cladding. Therefore, the bandgap allows light to propagate. We know that only photons with a bandgap larger than the cladding regions are allowed through the photonic crystal. This means that the photons that do not go through the core evanesce in the cladding zone.

2.2.3 Advantage of Photonic Crystal Fibers over Traditional Fibers:

- ✓ While traditional fibers rely on TIR for guiding the incident light, PCF can utilize index-guiding or photonic bandgap guiding or a combination of both to guide and confine light.
- ✓ Due to the larger core size and limited mode confinement, traditional fibers experience larger propagation loss and increased non-linear effects while PCFs have lower propagation loss and optimized non-linear effects owing to their compact mode confinement.
- ✓ Traditional fibers have limited control over their dispersion characteristics, but PCF offers flexible and customized dispersion mechanisms based on applications.
- ✓ Whereas standard fibers are primarily tuned for telecom wavelengths, PCF may operate in a wide variety of wavelengths from visible to infrared to UV.
- ✓ Unlike conventional fibers, whose refractive index profiles are fixed, PCFs' structural characteristics and air hole configurations may be modified to provide the appropriate optical qualities.

CHAPTER – 3

SURFACE PLASMON RESONANCE

3.1 Introduction:

Surface Plasmon Resonance (SPR) is a phenomenon that occurs when light incident upon a metal-dielectric surface, causing free electrons to collectively oscillate at the metal's surface. Surface plasmons are a collective oscillation that interact with incident light to produce an electromagnetic wave that travels along the metal-dielectric contact.

Surface plasmons are the quantized oscillations of free electrons confined to the surface of a metal. The interaction between incident light and the free electrons on the metal surface is what causes them to form. Resonance takes place when the incident light's frequency aligns with the surface plasmons' natural frequency, leading to a considerable absorption or dispersion of the incident light. SPR is an efficient technique for detecting and sensing molecular interactions because of this resonance condition's heightened sensitivity to alterations in the refractive index of the surrounding environment.

3.2 Working Principle of SPR

Surface Plasmon Resonance (SPR) involves the excitation and detection of collective motions of free electrons, known as surface plasmons, at a metal-dielectric interface. In SPR, Light from an outside source is directed towards a metal film using a prism., and at the resonance angle, it couples with the surface plasmons, exciting them. These excited surface plasmons then propagate along the metal surface, creating an evanescent electromagnetic wave that extends into the surrounding medium. A portion of the incident light is reflected back from the metal film, carrying valuable information about molecular interactions or changes occurring at the metal surface. By monitoring the intensity or angle of the reflected light, researchers can analyze binding events, affinity, and concentration of analytes in real-time. Changes in the reflected light signal indicate variations in the refractive index of the medium, providing insights into biochemical interactions and molecular

processes. SPR offers label-free and real-time detection of molecular interactions, making it a powerful tool in biosensing, drug discovery, and various other applications.
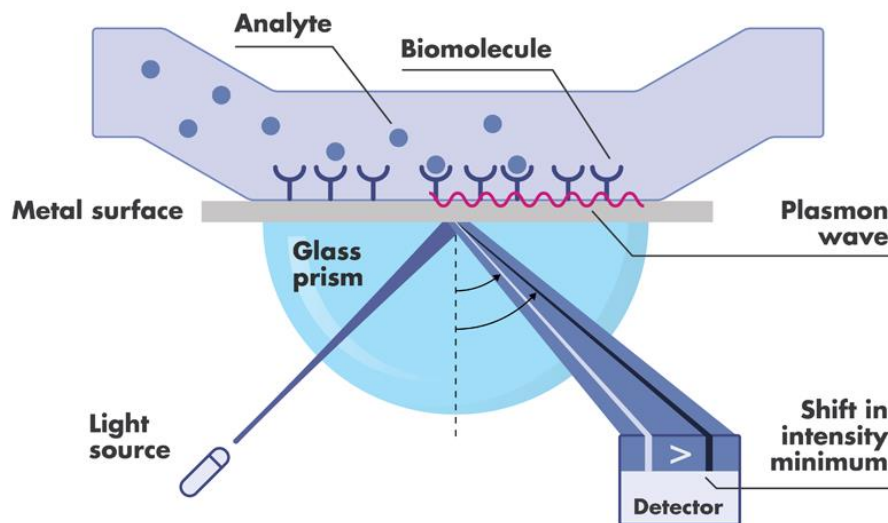
Figure 3.1: Creation of surface plasmons in a metal surface by the reflection and absorption of light

3.3 Surface Plasmon Wave:

A surface plasmon wave (SPW) is a collective oscillation of electrons at the interface between a metal and a dielectric or semiconductor material. It occurs when photons couple with the free electrons at the metal-dielectric interface, leading to the formation of a propagating wave that is bound to the surface. SPW exhibits unique properties such as strong confinement of the electromagnetic field to the interface and sensitivity to changes in the local environment. SPW plays a crucial role in various applications, including surface-enhanced spectroscopy, biosensing, nanophotonic, and plasmonic devices [66]. They enable the manipulation and control of light at subwavelength scales, opening up opportunities for compact and high-resolution optical technologies.

3.4 Evanescent Field:

When light is reflected at angles that are greater than the critical angle, a significant amount of its intensity is sent back into the medium that it is reflecting off of, known as the cladding. On the

other hand, a phenomenon known as the evanescent wave can be found close to contact. This is defined by the fact that the power of the wave decreases exponentially with increasing distance. For real-time surface-specific detection, this evanescent field, which only extends a short distance from the interface, has been brought to use. The whole internal reflection process in optical fibers directs the flow of light energy throughout the length of the fiber; however, a portion of the wave that is reflected internally travels past the core boundary and into the cladding. After the cladding has been removed, the evanescent wave will be able to propagate into the substances that are around it . This property of the evanescent wave may be controlled and in systems that contain an absorbing dielectric media, the powerful evanescent electric field boosts the medium's capacity to absorb electromagnetic radiation.
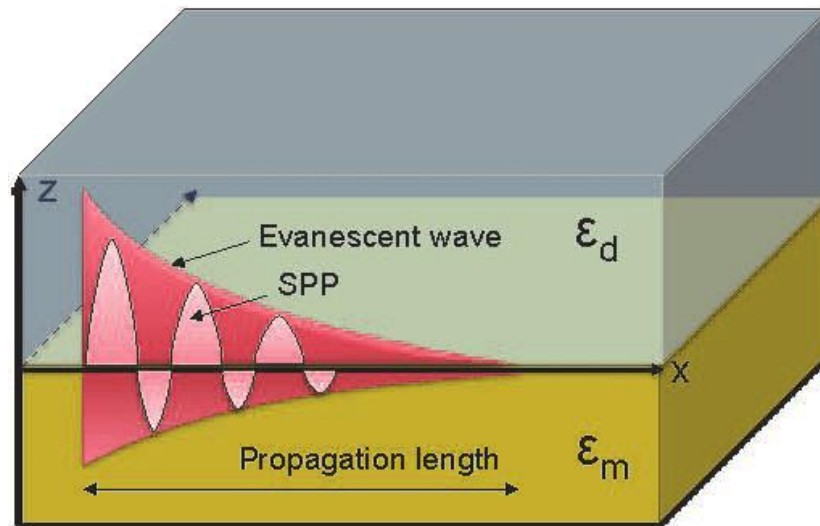
Figure 3.2: Evanescent wave

3.5 Advantages of SPR:

Surface plasmon resonance (SPR) offers a number of benefits in a wide range of situations, including:

➢ **Label-Free Detection:** SPR makes it possible to detect without using labels or markers made of molecules. This improves the experimental process, lowers expenses, and prevents any potential interference or analyte change.

- ➢ **Real-Time Monitorin**g: SPR provides real-time monitoring of molecular interactions, allowing researchers to observe binding events, kinetics, and affinity measurements as they occur. This enables dynamic and kinetic analysis of biomolecular interactions.
- ➢ **High Sensitivity:** At the metal-dielectric contact, SPR is extremely sensitive to changes in refractive index. It is excellent for applications like biosensing and drug discovery due to its sensitivity, which permits the detection of minor changes in analyte concentration.
- ➢ **Versatility:** Small molecules, proteins, nucleic acids, and nanoparticles are just a few of the many items that can be used using SPR. It can be applied to research DNA hybridization, antibody-antigen binding, protein-protein interactions, and more
- ➢ **Non-Destructive and Reusable:** SPR measurements can be repeated on the same sample without causing damage. As a result of its reusability and capacity to regenerate the sensor surface, SPR is a practical and sustainable method
- ➢ **Wide Range of Applications:** SPR has uses in a wide range of industries, including life sciences, biotechnology, pharmaceuticals, environmental monitoring, food safety, and material science. It offers useful details on surface phenomena, biomolecular recognition, and molecular interactions.

3.6 Localized Surface Plasmon Resonance

Localized Surface Plasmon Resonance (LSPR) is a phenomenon that occurs when noble metal nanoparticles, such as gold or silver, interact with light at specified wavelengths. On the surface of certain nanoparticles, it involves the collective oscillation of free electrons known as localized surface plasmons [67]. Numerous applications, including sensing, imaging, and nano-photonics, use LSPR.

The interaction between the incident electromagnetic field and the localized surface plasmons is the core of the LSPR's operation. When nanoparticles are illuminated with light, the collective oscillation of the free electrons is excited at a resonance frequency, resulting in a strong absorption and scattering of light at a specific wavelength. This resonance wavelength is highly sensitive to the size, shape, composition, and surrounding environment of the nanoparticles.

A change in the local refractive index occurs close to a nanoparticle when an analyte or molecule interacts with its surface. The resonance conditions are changed as a result, which shifts the LSPR wavelength. It is possible to identify and measure analytes with high sensitivity by maintaining an eye on this change in the nanoparticles' absorption or scattering spectrum.

The resonance wavelength of LSPR sensors is strongly influenced by nanoscale changes in the proximity of the nanoparticles, which accounts for their remarkable sensitivity. Because of this, LSPR is a wonderful platform for real-time and label-free sensing applications. The LSPR response can be tuned, enabling customized sensing platforms for certain analytes. This is made possible by the nanoparticles' capacity to be controlled in terms of size, shape, and surface characteristics.

3.7 Advantages of LSPR over SPR

Using LSPR instead of SPR offers several significant advantages. Some of the advantages are listed below:

1. **Simplified optical hardware:** LSPR eliminates the requirement for a prism, which lowers the instrument's complexity and price.
2. **Improved robustness:** LSPR provides more accurate measurements since it is less sensitive to mechanical noise and vibration.
3. **Reduced sensitivity to variations in the bulk refractive index:** LSPR is less sensitive to changes in the bulk refractive index, reducing the possibility of experimental data mistakes.
4. **No strict temperature control requirements:** Unlike SPR, LSPR does not require precise temperature control, allowing instrument setup and operation simpler.
5. **Cost-effective sensor chips:** Because LSPR sensor chips can be produced at a cheaper price, they are more readily available and economical.
6. **User-friendly and easier maintenance:** Simple setup and less susceptibility to environmental conditions make LSPR equipment easier to use and maintain

CHAPTER – 4

ANALYSIS OF SPR-LSPR BASED PCF SENSORS

4.1 Outline:

PCF sensors have attracted the interest of researchers for quite some time because of their higher sensitivity and lower resonance peak. To use the PCF as a sensor, the phenomenon of SPR is utilized. The integration of the SPR concept with PCF structures has enlarged the horizon of sensing. PCF sensors are now used in label-free detection [68], [69], environmental monitoring [70], water testing, liquid and gas sensing [71], biosensing [72], milk sensing [12], blood component detection [13], [14], [73], THz frequency sensors [74]–[84] and many more.

When an incident light travels through the structure, SPR takes place in PCF sensors based on SPR [85]. The surface plasmon wave (SPW) is produced when the metal's surface is subjected to an induced evanescent field, which in turn causes the free electrons on the plasmonic layer to oscillate. In order to establish phase-matching between the modes, surface plasmons must be excited and the Surface Plasmon Polariton (SPP) and core mode must combine at a specified wavelength. A strong resonance peak forms at that wavelength, which depends heavily on the RI of the analyte [24].

In the case of LSPR, a coherent excitation of conduction band electrons occurs within the nanoparticle junctions. [86]. There has been a shift in recent years toward LSPR-based works rather than SPR-based ones because of the shorter decay length of the EM field [85], increased sensitivity, response speed, and throughput [87]. The lack of a coupling method for surface excitation also makes LSPR sensors suitable for miniaturization, leading to compressed sensing technology.

In this chapter, we will investigate various shapes and structures of PCF sensors that have been used till date and some forms of sensing methods.

4.2 Prism based Sensors:

The prism shaped sensors were the first mechanism which used SPR phenomenon to detect unknown analytes. This started with Liedberg et al. in 1983, when he developed the prism coupled SPR sensor for sensing unknown biomolecules [88]. Prism-based sensors have a sensing surface made from a metal film placed on a glass prism. The prism acts as a coupling device, directing light at an angle equal to the resonance angle into the metal-dielectric contact. As soon as the resonance condition is satisfied, surface plasmons are excited, and the reflected light intensity displays a sharp dip. Later, it became clear that prism-based SPR sensors were ill-suited for remote-sensing because of drawbacks such as inaccurate sensing application and excessive bulk brought on by additional complex opto-mechanical elements [89], [90].
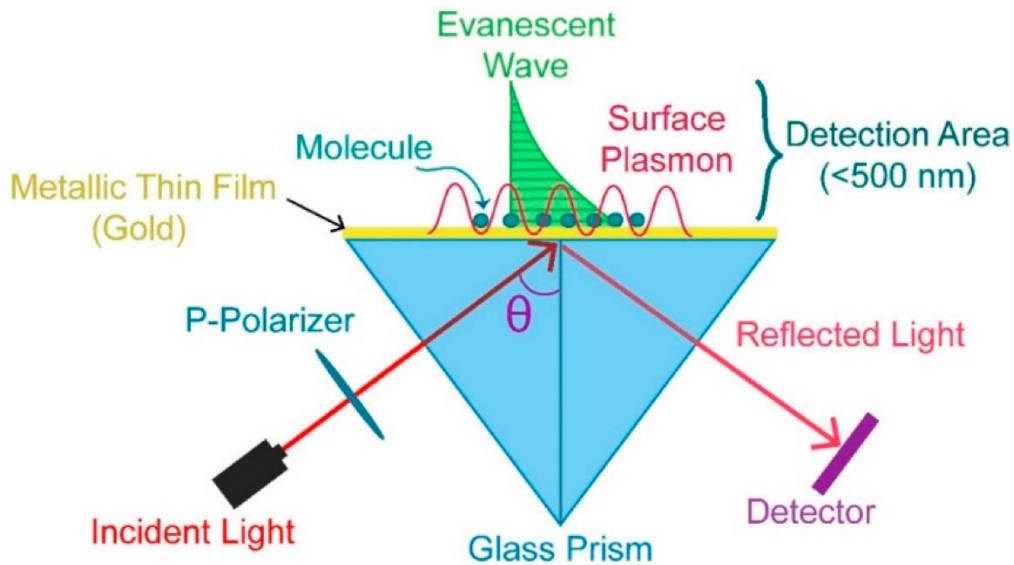
Figure 4.1: Prism based SPR sensor

4.3 Internal Sensing Approach:

Internal sensing type sensors were developed to overcome the difficulties of prism-based sensors. In this method, analytes are packed inside of air holes that have been coated with metal films [90], [91]. As it is challenging to coat the internal fiber holes with metal coatings and load them with analytes, putting a system of this type into practice is difficult. The miniscule dimensions of the holes are the reason for these complications. Furthermore, it is not possible to fabricate holes of

consistent thickness. The constant process of measuring, emptying and refilling consumes a lot of time and furthermore may instigate degradation in the quality of the sensor.
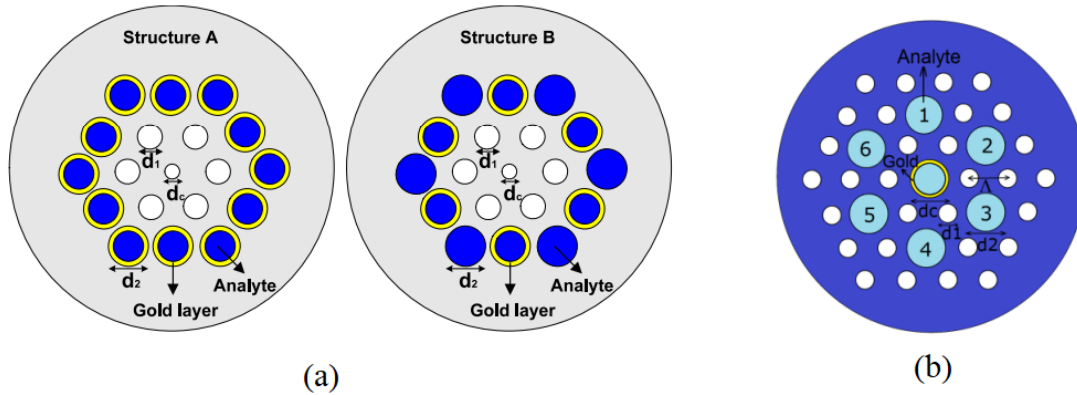
Figure 4.2: PCF sensors based on Internal sensing approach

4.4 External sensing approach:

External sensing in PCF sensors implies a way of detecting the target analyte or parameter outside of the PCF structure. Light is guided to the sensing zone by the PCF, which also works as a waveguide to collect the signal and send it back to the detection system. Applications where direct contact with the analyte is not desirable or possible can benefit from these techniques since they allow for remote and non-invasive measurements. Several structures have been investigated over the years for achieving the utmost sensitivity. Some of them will be discussed here:

4.4.1 D-Shaped Structure:

The shortcomings of prism-based sensors and internal sensing-based sensors can be mitigated by the use of D-shaped or exposed-core PCFs. In 2017, Wu et al. proposed an ultrasensitive and broadly detectable RI sensor based on a D-shaped PCF [figure 4.3 (a)]. In order to avoid the difficulties faced when plasmonic material is filled on the air hole, the gold layer is laid on the smooth, polished surface. The sensor displayed a high sensitivity of 31,000 RIU/nm with a broad range of analyte detection from 1.32 – 1.40 [92].

M. E. Rahaman and his team worked on a D-shaped PCF sensor to diagnose glucose levels in the human body [figure 4.3 (b)]. The developed sensor was tested for a long RI range extending from

1.18 – 1.36. It showed a maximum wavelength sensitivity (WS) of 3,000 nm/RIU and an amplitude sensitivity (AS) of 243 RIU^{-1}. The sensor showed a resolution of 3.341×10^{-6} RIU [93].

In 2018, E. Haque et al. designed a D-shaped sensor which had the potential to a WS of 20,000 nm/RIU and a corresponding AS of 1054 RIU^{-1} [figure 4.3 (c)]. The sensor could function in an analyte range of 1.18 – 1.36. Gold was chosen as the plasmonic material to develop the SPR phenomenon [94].
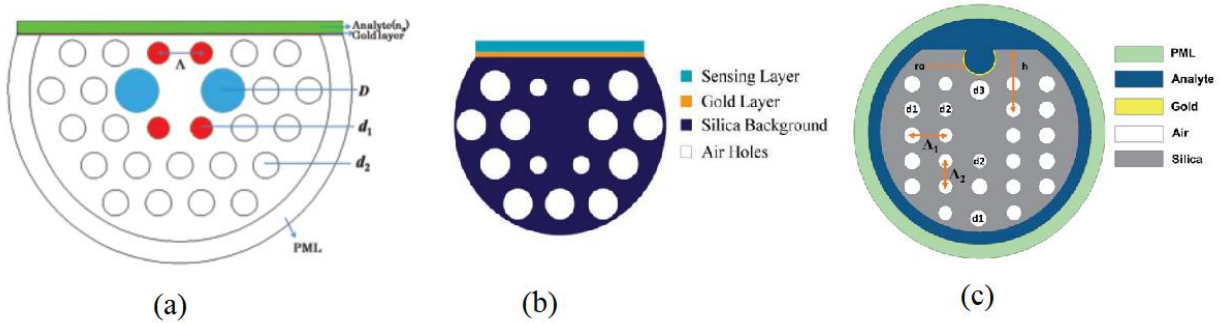
Figure 4.3: D-shaped PCF sensors

Even though D-shaped PCF can reduce the sensing complexity incurred by internal sensing sensors, they present a fabrication challenge because their flat portion must be polished. However, in fact, this form of sensor requires etching of specific areas of the surface, which further increases fabrication complexity and sensor costs.

4.4.2 Circular Lattice Structures:

Circular lattice structures are easy to design and can be fabricated as the plasmonic layers are implanted outside the PCF structures. Md. Abdul Khalek et al. devised a circular lattice PCF which uses the SPR phenomenon to function. The sensor was investigated from a range of 1.34 – 1.37 and a maximum WS of 9000 nm/RIU and an AS of 318 RIU^{-1} was found [95]. The sensor configuration is shown in figure 4.3 (a).

Q. M. Kamrunnahar and her team proposed a circular structured PCF sensor which was able to display a WS of 11,200 nm/RIU and a corresponding AS of 505.037 RIU^{-1} from an analyte range of 1.33 to 1.44 [96]. It is shown in figure 4.3 (b).
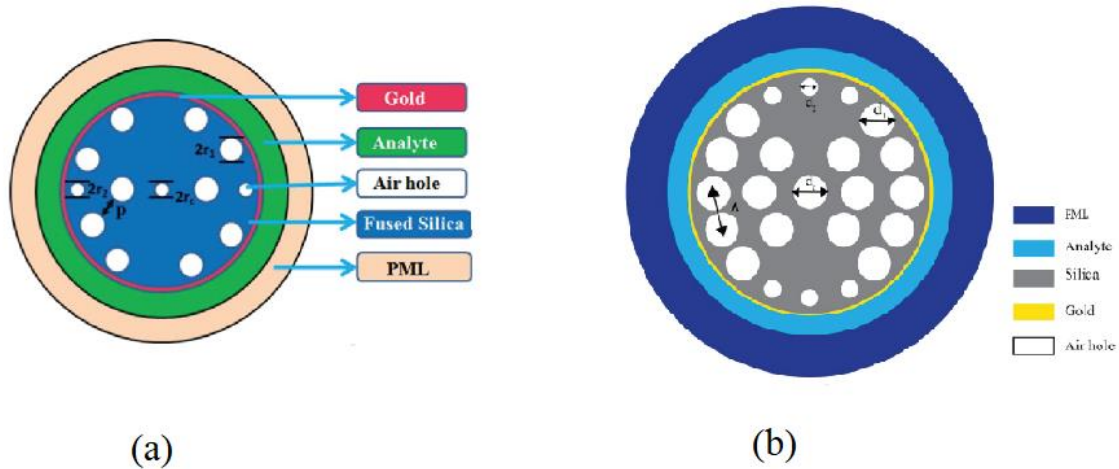
Figure 4.4: Circular lattice PCF sensors

4.4.3 Hexagonal Lattice Structures:

The hexagonal structure is defined based on the arrangement of the air holes in the cladding region. S.M. Abu Sufian Sunny et al. formed a PCF sensor with WS of 29,500 nm/RIU and an AS of 3060 RIU^{-1}. Several air holes of varying diameters were arranged in a hexagonal pattern around a central air hole while the gold layer was deposited outside the PCF [figure 4.5 (a)]. The sensor showed to work in an RI range of 1.33 – 1.43 [97].

Md. Mahbubur Rahman et al., in 2020, devised a PCF sensor based on SPR with hexagonal arrangement of air holes [figure 4.5 (b)]. The sensor displayed a maximum WS of 13,000 nm/RIU and an AS of 953.23 RIU^{-1} within a range of 1.33 – 1.37 RI [98].
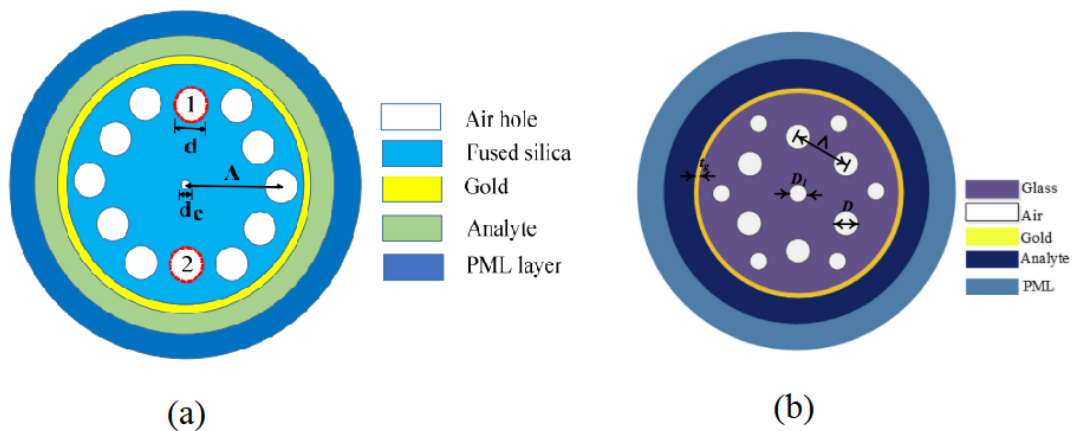
Figure 4.5: Hexagonal lattice PCF sensors

4.4.4 Square, Spiral and Trapezoidal Structures:

Md. Nazmul Hossen et al. proposed a sensor which featured two layers of square air holes arranged in a symmetrical pattern [figure 4.6 (a)]. Therefore, an even greater evanescent field was produced by including a small air vent in its core. The central air hole in the multiple layers is intentionally narrower than the others. The proposed sensor was built so that connection between the core and SPP mode is possible to boost sensitivity. Gold was chosen as the plasmonic material to detect unknown analytes. The highest WS the sensor could uphold was 6000 nm/RIU and an AS of 442.11 RIU^{-1} [99].

Md. Rabiul Hasan developed a rather unique SPR-PCF sensor where gold was chosen as plasmonic material for external sensing. The structure comprised of three rings and six arms, with the first ring intentionally designed with two missing air holes along the horizontal axis to create birefringence asymmetry. This configuration enhances the coupling between the x or y polarized mode and the surface plasmon polariton (SPP) mode, resulting in improved sensing performance [figure 4.6 (b)]. The sensor's sensing performance was a WS of 4600 nm/RIU and AS of 420.4 RIU^{-1} [100].

Suoda Chu proffered a novel sixfold photonic quasi-crystal fiber (PQF) with a trapezoidal analyte channel for SPR sensing where gold was to detect analytes [figure 4.6 (c)]. Unlike conventional D-shaped PCFs, they incorporated a trapezoidal analyte tube to study the position of the sample liquid height and assess fabrication method functionality. This unique design, consisting of four layers of air holes, offered advantages such as low confinement loss and a flattened zero-dispersion profile across a broader wavelength range [101].

(a) Square shaped   (b) Spiral shaped   (c) Trapezoidal shaped
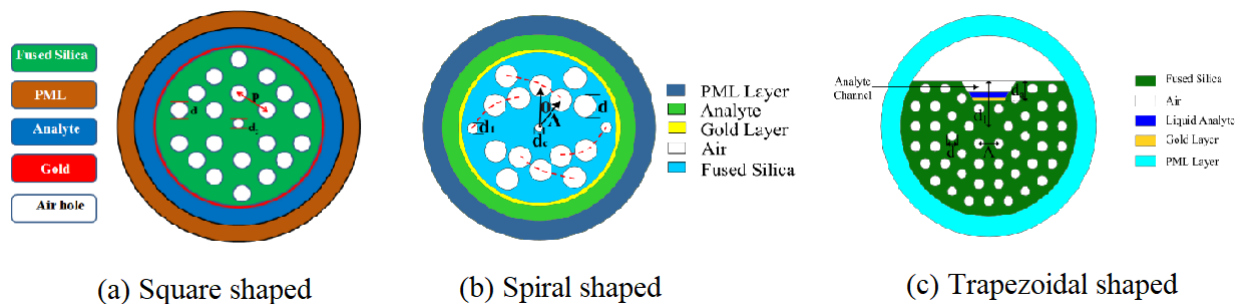
Figure 4.6: (a) Square shaped PCF (b) Spiral shaped PCF (c) Trapezoidal shaped PCF

CHAPTER - 5

PLASMONIC MATERIAL SELECTION:

5.1 Factors to Consider while Selecting Plasmonic Material:

The selection of plasmonic material is a crucial step in the design of SPR/LSPR-based sensors. The surface plasmon resonance (SPR) is generated in a significant way by the plasmonic material. At the boundary between a plasmonic material (usually a metal) and a dielectric medium, electrons in the plasmonic material collectively oscillate. Surface plasmon resonance (SPR) is excited when light strikes a plasmonic substance at a particular incidence angle and wavelength. The optical features of the plasmonic material, such as its refractive index, electron density, and conductivity, determine the resonance conditions for SPR. When incoming light interacts with a plasmonic material, an evanescent field is formed at the metal-dielectric interface that is very sensitive to variations in the refractive index of the surrounding environment. The SPR response changes when the refractive index at the surface of the plasmonic material changes due to the binding of target analytes or changes in the nearby environment. Analyte interactions can be detected and characterized by monitoring the intensity of light as it interacts with the sample.

However, some key factors need to be taken into account in order to choose the optimum plasmonic material for a given application. Some of them are:

❖ **Plasmonic Properties:** Plasmonic materials can detect and analyze analytes using strong surface plasmon resonance (SPR) and other optical characteristics. Selecting a material with a plasmon resonance wavelength suitable for excitation and interaction with the target analyte improves a sensor's sensitivity and specificity.

❖ **Stability and Durability:** Plasmonic materials should be chemically stable and durable. A stable plasmonic substance keeps PCF sensors performing well over time despite exposure to numerous analytes or environmental conditions.

❖ **Refractive Index Sensitivity:** Changes in the refractive index close to the detecting region are used by plasmonic PCF sensors to detect analyte binding or environmental changes. For strong plasmon-analyte interaction and a highly sensitive sensor, the plasmonic material should be responsive to variations in refractive index.

- ❖ **Fabrication Compatibility:** Manufacturing PCFs necessitates the use of appropriate plasmonic materials. The material should not damage the sensor's integrity or performance when deposited or incorporated into the PCF framework.
- ❖ **Cost and Availability:** For real-world applications, it's important to think about price and availability. By selecting low-cost and plentiful plasmonic materials, PCF sensors might be scaled up and brought to market.

5.2 Common Plasmonic Materials:

Metallic components are often used in plasmonic devices because of the abundance of free electrons in these materials, which is the source of the plasmon phenomena at optical and telecommunication frequencies. The negative real permittivity required of all plasmonic materials is provided by these free electrons [102]. Metals like gold (Au), silver (Ag), and copper (Cu) are frequently employed because of their plasmonic properties. Due to its larger resonance shift and compatibility with biomolecules and biochemicals, gold is typically chosen above other materials [41]. However, there are a number of issues that arise when the layer thickness of gold is altered. The AS decreases smoothly with increasing thickness [103] and abruptly below 10 nm, indicating a discontinuous layer [104]. Gold's heat evaporation process also makes its price prohibitive and its surface harsh [105]. Silver, on the other hand, is cheaper, has a higher quality factor than any other metal [102], has a resonance peak that is much more compelling than that of other plasmonic materials, and opposes low optical damping and zero interband transitions much like gold [106]. Semiconductors show considerable potential as plasmonic materials because of their easy manufacture and the flexibility to tune features like carrier concentration. To achieve low loss plasmonics in the optical frequency range, a highly doped, broad bandgap semiconductor with outstanding carrier mobility emerges as a top choice. Some common semiconductors used in optical fiber fabrication are Aluminium doped Zinc Oxide (AZO), Gallium doped Zinc Oxide (GZO), Indium Tin Oxide (ITO), etc.

5.2.1 Gold based Sensors:

Figure 4.3, 4.4, 4.5 and 4.6 all show the use of various gold-based sensors. The sensors all exhibit a number of advantages like strong plasmonic resonance, high stability, low absorption loss, biocompatibility and fabrication flexibility.

5.2.2 Silver based Sensors:

Silver based sensors are also very popular because of the advantages they provide as explained in section 5.2. Han et al. proposed a birefringence PCF based SPR sensor with silver [figure 5.1 (a)] and obtained a WS of 16, 700 nm/RIU within a detection limit of 1.33-1.42 and a corresponding sensor resolution of 5.99×10^{-6} RIU [107]. Momota et al. suggested a hollow core circular lattice PCF where silver is used as plasmonic material [figure 5.1 (b)] and obtained a result of 4200 nm/RIU WS, 300 RIU^{-1} AS and a sensor resolution of 2.38×10^{-5} RIU and 3.33×10^{-4} RIU respectively, working in the range of 1.33-1.37 RI [108]. Kumar et al. worked on a PCF sensor based on silver [figure 5.1 (c)] thin film that operates within 1.25-1.30 RI and obtained a WS of 1932.09 nm/RIU and a sensor resolution of 3×10^{-5} RIU [109].

(a) (b) (c)
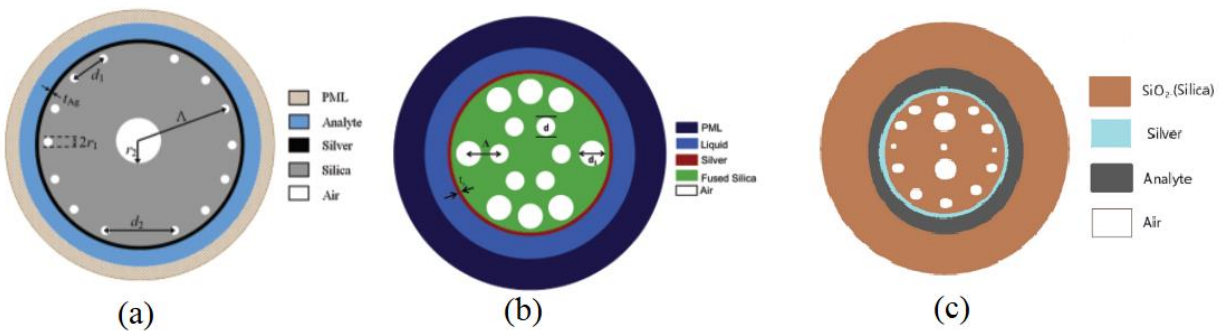
Figure 5.1: Silver based PCF sensors

5.2.3 AZO based Sensors:

AZO (aluminum-doped zinc oxide) is a viable solution for expanding the wavelength range of plasmonic materials. Due to its low charge carrier density and plasma frequency, AZO is effective at longer wavelengths, particularly in the near-infrared (NIR) range. Because of this property, AZO is an attractive option for plasmonic applications that call for a broad wavelength coverage. The

AZO Coated PCF-SPR sensor suggested by Jitendra Narayan et al. [figure 5.2] is capable of detecting light between 1600 and 2000 nm in wavelength and has a maximum wavelength sensitivity of 5000 nm/RIU when working in y-polarization mode [110].
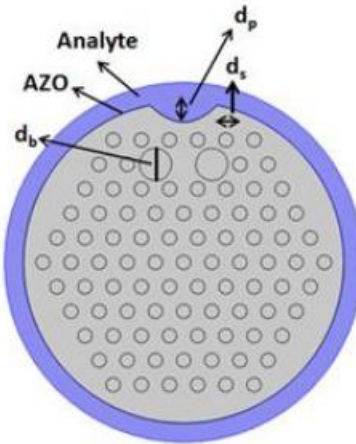
Figure 5.2: AZO based PCF sensor

5.2.4 GZO based Sensors:

The exceptional characteristics of GZO (gallium-doped zinc oxide) as an alternative plasmonic material, such as its durability, cost-effectiveness, minimal doping requirements, and low losses at telecommunication wavelengths, position it as the leading choice in the field. Exploring a sensor using GZO as the plasmonic material has the potential to achieve extraordinary performance attributes such as increased sensitivity, an ultra-wide detection range for refractive index (RI) spanning low and high values, and reduced crosstalk (CL). K M Mustafizur Rahman et al. designed a GZO based PCF-SPR sensor with ultra-wide refractive index sensing owing to a WS of 17000 nm/RIU, AS of 135 RIU^{-1} and the corresponding sensor resolutions of $5.88 \times 10-6$ RIU^{-1} and $7.36 \times 10-6$ RIU respectively, ranging from 1.24-1.40 RI [111].
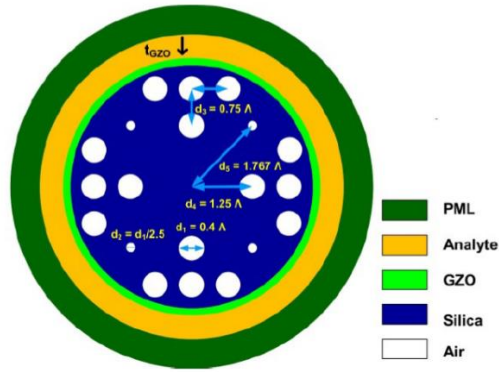
Figure 5.3: GZO based PCF sensor

5.2.5 Bimetallic Materials based Sensors:

The advantages of using bimetallic materials in PCF sensors include the capacity to tune plasmonic characteristics, a wider wavelength range, a stronger plasmon field, greater stability, and increased surface sensing. These characteristics make bimetallic materials a promising option for improving sensing performance in PCF-based plasmonic sensors. Again, a coating of graphene or TiO_2 over the layer of gold or silver can help protect the valuable metallic layers from corrosion and oxidation. There have been instances of using gold-graphene layer, silver-graphene, silver-TiO_2, silver-TiN combinations to protect the gold/silver layer as well as enhancing the sensing properties of the PCF sensor.

5.2.5.1 Bimetallic Silver-Graphene based Sensors:

Tianshu Li et al. recommended a refractive index (RI) sensor in the form of an H-shaped photonic crystal fiber (PCF) covered with Ag-graphene layers and featuring an open structure defined by U-shaped grooves [figure 5.4 (a)]. Maximum WS is determined to be 12,600 nm/RIU over a broad analyte RI range of 1.33 to 1.41 [112].

The D-shaped sensor proposed by Jitendra Narayan Dash et al., which uses an Ag-graphene combination, has a WS of up to 3700 nm/RIU and a resolution of up to 2.7×10^{-5} RIU [113]. It is shown in figure 5.4 (b).
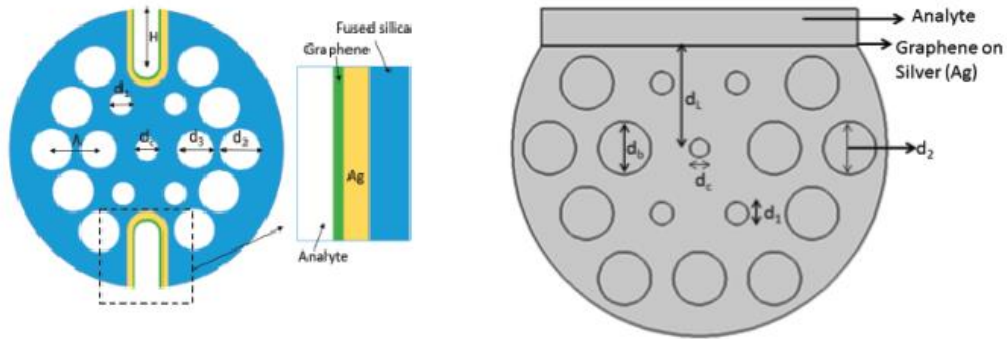
Figure 5.4: Ag-graphene combination PCF sensors

5.2.5.2: *Bimetallic ITO-ZnO based Sensor:*

The sensor suggested by Kaur et al., which makes use of ITO and ZnO to improve coupling, has a WS of 10,000 nm/RIU and a resolution of 2×10^{-5} RIU [114]. It is shown in figure 5.5.
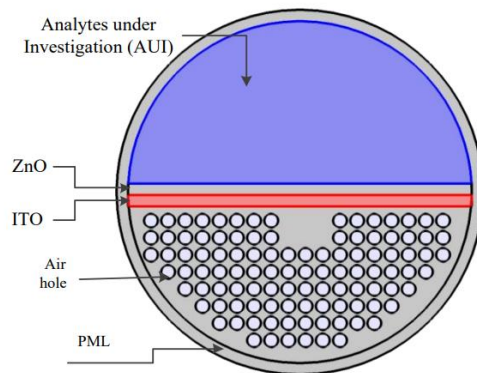
Figure 5.5: ITO-ZnO based PCF sensor

5.3 Dual Plasmonic Material based Sensors:

The bimetallic materials-based sensors discussed in sector 5.2.5 were all incorporated for more enhanced sensing performance or protecting the gold/silver layer. From 2022, there were a new field of research undertaken where two separate plasmonic layers were used distinctly to analyze analytes within the same refractive index. This concurrent use of plasmonic layers enable to sensor to display two distinct loss peaks within the same refractive index where both the loss peaks are used to detect the unknown material.

5.3.1 Dual Plasmonic Layered PCF sensor based on Au-AZO:

In this paper, a novel sensor based on LSPR effect is described using both Au and AZO as plasmonic materials. As a result of this interaction, a novel dispersion relation has emerged, and two different resonance peaks have been identified. The simulation results show that by optimizing the structural parameters, this sensor may achieve excellent sensing performance. Two different type of sensor structure was proposed here and the parameters were optimized by switching the positions of the Au and AZO layers as shown in the figure 5.6 (a). The sensor's maximum AS is 8485.2 RIU^{-1} when AZO is employed as the intermediate plasmonic material, and its maximum WS is 46300 nm/RIU in the y-polarization direction. Not only that, but it can resolve wavelengths to an accuracy of 2.16 x 10^{-6} RIU and amplitudes to an accuracy of 1.18 x 10^{-6} RIU. The sensor has a high figure of merit (2923.2), suggesting first-rate detection precision, and shows great linearity (R2 = 0.99312). In addition, it is sensitive enough to identify unnamed analytes throughout a broad refractive index range (1.27–1.45). Consider the double peaks together for neighboring refractive indices, and the sensor shows a maximum sensitivity of 4400 nm/RIU for x-polarization mode and 16500 nm/RIU for y-polarization mode, according to the study's newly introduced sensing metric termed double peak shift sensitivity. The versatility of its twin peak sensor design makes it well suited for the sensitive and specific detection of a wide range of biological organic substances [115].

5.3.2 Dual Plasmonic Layered PCF sensor based on GZO-AZO:

In this work, the authors suggested the use of aluminum-doped zinc oxide (AZO) and gallium-doped zinc oxide (GZO) in parallel to create a sensor [figure 5.6 (b)] that operates on the principle of localized surface plasmon resonance (LSPR). Different resonance peaks and a novel dispersion relation are displayed by the sensor as a result of its arrangement of two plasmonic materials. The novel parameter introduced in [15] double peak shift sensitivity, was used to optimize the design parameters. The sensor parameters which showed the highest of DPSS was taken as the final value. The suggested sensor has the capacity to detect unknown analytes with a double peak shift sensitivity of 10,890.35 nm/RIU in the RI range of 1.30 to 1.41. It has a high figure of merit (1558.83) and impressively high amplitude and spectral sensitivities (11,609.67496 RIU^{-1} and 11,088.5 nm/RIU, respectively). The sensor has a maximum limit of detection (LOD) up to the order of 10^{-11}, with a maximum amplitude resolution of 8.614 x 10^{-7} RIU and a maximum

wavelength resolution of 9.874 x 10^{-6} RIU. Because of the limits of traditional plasmonic metals like gold and silver, this sensor presents a new method for investigating biological analytes such cancer cells, malaria-infected phases, and blood components [67].

5.3.3 Dual Plasmonic Layered PCF sensor based on GZO-Au:

Using gallium-doped zinc oxide (GZO) and gold as plasmonic materials, the researchers offer a sensor based on LSPR technology [figure 5.6 (c)]. The combined usage of these materials causes the sensor design to display dual resonance peaks at separate wavelengths. The unique parameter, Double Peak Shift Sensitivity (DPSS) discussed in [15], is presented and utilized to fine-tune the sensor's structural properties for maximum performance. The highest DPSS calculated with COMSOL Multiphysics simulation was 11,720 um/RIU. Analytes having refractive indices between 1.30 and 1.40 can be detected over a wide range with the suggested sensor. With a WS of 11,480 nm/RIU and a resolution of 8.71×10^{-6} RIU, it is capable of detecting analytes in the ultraviolet and visible light spectra. The sensor's low confinement losses allow for a broader range of lengths across which it can function. This innovative design has the potential for several applications in the ultraviolet and visible light spectrums, including very accurate biosensing [116].
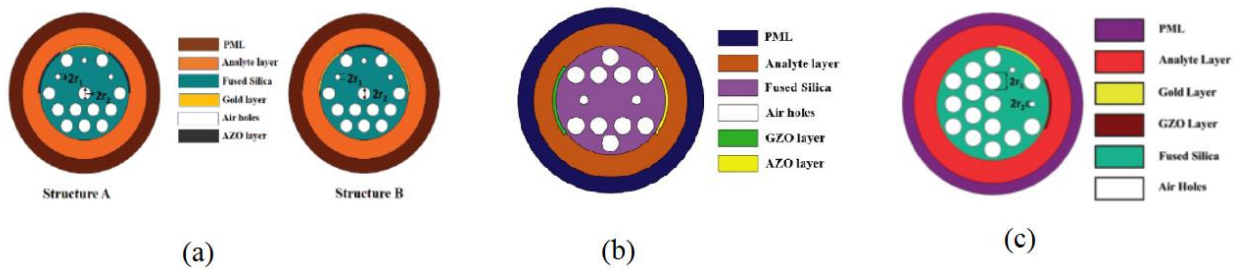
Figure 5.6: (a) AZO-Au based PCF sensor (b) GZO-AZO based PCF sensor (c) GZO-Au based PCF sensor

Thus, from the discussion in section 5.3, utilizing dual plasmonic layers offers exciting prospects for cutting-edge research by enabling enhanced control over light-matter interactions and expanding the range of achievable functionalities in various applications.

CHAPTER – 6

MATHEMATICAL MODELING AND MATERIAL SPECIFICATION

6.1 Introduction:

In this chapter, we have discussed the various materials that are involved in developing PCF sensors based on SPR effect. Some examples of these materials are Silica (SiO2), Silver (Ag), and Gallium-doped Zinc Oxide (GZO). Considering its direct relationship to the sensing properties, the refractive index (RI) has been our primary focus in characterizing these materials on simulation platforms. Since the RI is equal to the square root of the permittivity, we have provided both the RI and permittivity equations for these materials. In addition, we have investigated a wide range of factors that can impact sensor performance. Confinement loss (CL), amplitude sensitivity (AS), wavelength sensitivity (WS), resolution, FOM, and sensor length are all examples of such metrics. The formulas for calculating these parameters are presented and discussed in this chapter. We can improve the performance of SPR-based PCF sensors by understanding and manipulating these parameters.

6.2 Characterization of Materials:

The equations used to characterize materials are discussed here. Only the materials discussed during the course of the research works explained in chapter 7 have been included here. It is to be noted that some materials have a complex effective RI. Any material's effective RI can be written in the complex form neff = n + jk, where n and k represent the real and complex parts of the RI, respectively.

6.2.1 Silver:

The choice of the right plasmonic material is a key step in developing SPR/LSPR-based sensors. Gold is often preferred due to its higher resonance shift and compatibility with biomolecules and biochemicals [41]. However, adjusting the thickness of the gold layer presents challenges [103]. The AS decreases gradually with increasing film thickness, while the film becomes discontinuous below 10 nm [104]. Gold is also disadvantageous due to its high cost and surface roughness resulting from thermal evaporation [105]. Silver, on the other hand, can be used as an alternative

to gold. The advantages that silver provides due to which we have given preference to it [102], [106]:

- ❖ Silver is a cost-effective alternative to gold in plasmonic material selection.
- ❖ Silver outperforms other metals in terms of quality factor.
- ❖ Silver exhibits a sharper resonance peak compared to other plasmonic materials.
- ❖ Silver has low optical damping and zero interband transitions, similar to gold.

The dielectric constant of silver is given according to the Drude-dispersion model [117]:

$$\varepsilon_{Ag} = 1 - \frac{\lambda^2 \lambda_c}{\lambda_p{}^2 (\lambda_c + i\lambda)} \qquad (6.1)$$

Where ε_{Ag} is the dielectric constant of silver, λ is the wavelength in free space, $\lambda_c = 17.614$ µm being the collision wavelength, and $\lambda_p = 0.14541$ µm which is the plasma wavelength.

6.2.2 Gallium doped Zinc Oxide (GZO):

Gallium doped Zinc Oxide, also known as GZO, is another plasmonic material used as a potential replacement for Ag or Au. In recent work, these transparent conductive oxides (TCO) have demonstrated promising results. GZO (Gallium-doped Zinc Oxide) offers several benefits over other plasmonic materials [118] -

- ❖ **Low Loss:** GZO generates less loss than other plasmonic materials, which enhances sensor performance and sensitivity.
- ❖ **Higher Figure of Merit (FOM):** GZO exhibits a higher Figure of Merit in the near-infrared (NIR) region, indicating that it is more effective at detecting analytes and has improved sensing capabilities.
- ❖ **Cost-effectiveness:** GZO is used in sensor designs as a replacement for expensive materials like gold and silver to reduce production costs without sacrificing performance.
- ❖ **High Carrier Concentration:** GZO emerges as an excellent choice as a plasmonic material due to its remarkable high carrier concentration, making it highly conducive to efficient plasmon generation and manipulation.

In case of GZO, the dielectric constant is formulated from the equation given by [118]:

$$\varepsilon_{GZO} = \varepsilon_b - \frac{\omega_p^{\ 2}}{\omega(\omega + i\gamma_p)} + \frac{f_1\omega_1}{(\omega_1^2 - \omega^2 - i\omega\gamma_1)} \qquad (6.2)$$

Where ε_{GZO} denotes the dielectric constant of GZO. The Lorentz-Drude parameters for GZO are listed in table 6.1:

TABLE-6.1: LORENTZ-DRUDE PARAMETERS FOR GZO

Parameter	GZO
ε_b	3.2257
$\omega_p[eV]$	1.9895
$\gamma_p[eV]$	0.1229
f_1	0.3859
$\omega_1[eV]$	4.050
$\gamma_1[eV]$	0.0924

6.2.3 Silica (SiO2):

Sensors based on SPR are typically made by coating PCF with a layer of plasmonic metal. Glass or plastics can be used to construct the PCF itself. The material of preference for PCF backgrounds is fused silica, also known as silicon dioxide. Due to its many beneficial characteristics, undoped silica is widely employed for this purpose [119].

❖ Silica offers excellent optical transparency at a wide range of wavelengths.

❖ It exhibits exceptional chemical stability and does not exhibit hygroscopic behavior.

❖ In terms of mechanical strength, silica excels; it can't be bent or pulled in any appreciable way.

❖ In the near-infrared spectral region, it has low scattering and absorption loss (approximately 0.2 dB/km), as illustrated in Figure 6.1.

❖ Exceptional performance is achieved through fusion splicing of silica materials.

❖ At high temperatures, silica can be drawn into fibers that are then used in manufacturing.

❖ Since silica has a relatively high damage threshold, laser-induced breakdown is less likely to occur. In fiber amplifiers, this quality is especially useful during the amplification of short pulses.
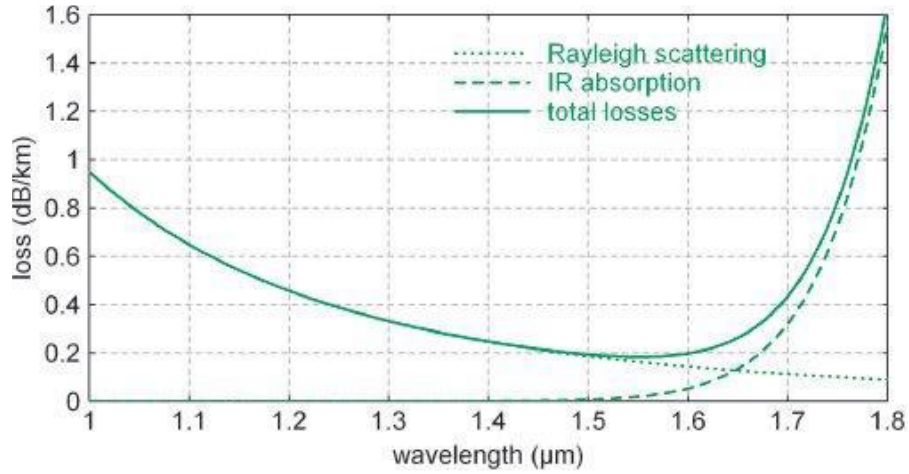
Figure 6.1: Intrinsic losses of Silica

The refractive index (RI) of fused silica is determined using the Sellmeier equation provided below, allowing us to derive its RI property:

$$n_{silica}(\lambda) = \sqrt{1 + \frac{B_1\lambda^2}{\lambda^2 - C_1} + \frac{B_2\lambda^2}{\lambda^2 - C_2} + \frac{B_3\lambda^2}{\lambda^2 - C_3}} \qquad (6.3)$$

Here, the refractive index (RI) of silica, represented as n_{silica} is dependent on the wavelength of light (λ) and the specific Sellmeier constants. It can be calculated with equation (6.3), and the Sellmeier constants listed in Table 6.2 This equation operates at a constant temperature of 25 °C [120], and it is important to note that its validity spans a wavelength range of 0.22 μm to 3.71 μm [121]. The relationship between silica's refractive index and wavelength is shown in Fig. 6.2. Notably, the imaginary part of the refractive index of silica is always zero, meaning that the refractive index of silica is always a real number.

Constant	Value
B_1	0.69616300
B_2	0.407942600
B_3	0.897479400
C_1	0.00467914826 μm^2
C_2	0.0135120631 μm^2
C_3	97.9340025 μm^2
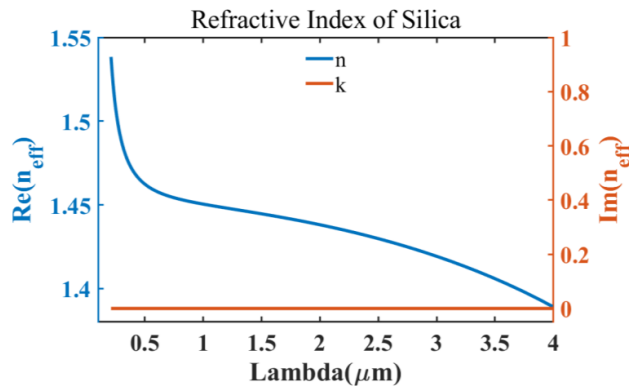
Figure 6.2: The refractive index of silica (at 25 degrees Celsius) vs light wavelength

6.2.4 Air:

Air is used to fill the voids within the Photonic Crystal Fiber (PCF) as its refractive index is close to 1, which means that light travels through it at the same speed it would in a vacuum. Air's constant refractive index allows for the detection of refraction with respect to the path of light in air. Refraction experiments based on Snell's Law are conducted in the atmospheric conditions surrounding us.
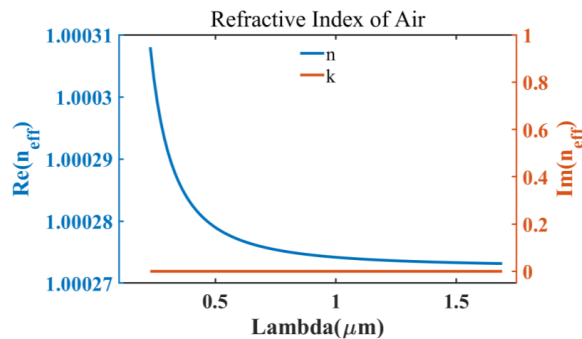
Figure 6.3: Refractive index of air vs wavelength of light

As can be seen in Figure 6.3, the refractive index of air changes very slightly as a function of the wavelength of the incident light. The figure highlights that the refractive index of air is real and stays very close to 1. So, the RI of air was set as 1 for all calculations in our study.

6.3 Performance Parameters:

Different performance parameters that are utilized for evaluating sensor performance have been covered in this section. These variables include confinement loss (CL), amplitude sensitivity (AS), wavelength sensitivity (WS), resolution, figure of merit (FOM), and others.

6.3.1 Confinement Loss (CL):

Since it is necessary to measure all other performance metrics, confinement loss (CL) is the parameter that is most crucial for assessing sensor performance. The CL denotes the energy that is switched from core mode to SPP mode. Losses caused by the leaky nature of the modes and the imperfect structure of the PCF fiber are known as confinement losses. A portion of the light energy that is transmitted through the PCF sensor's core seeps out and reaches the metal layer region. The term "confinement loss" (CL) refers to the total amount of this energy leak. The following equation ref-Sajjad [24], [121] can be used to calculate the CL:

$$\alpha = 8.686 \times k_0 \times \text{Im}(n_{eff}) \times 10^4 \, (dB/cm) \tag{6.4}$$

The wavelength is represented in the above equation, and $\text{Im}(n_{eff})$ stands for the imaginary part of the effective RI, n_{eff}. In addition, k_0 denotes the wavenumber and can be expressed as $k_0 = \dfrac{2\pi}{\lambda}$. The resonance state, where the frequencies of the transmitted light and the electrons in the plasmonic material are equal, is where the maximum CL is found. The "resonance wavelength" is the wavelength that causes resonance. The phase-matching condition is the state where the effective RI's real component of the core mode and the SPP mode are equal at resonance wavelength.

6.3.2 Amplitude Sensitivity (AS):

Amplitude interrogation (AI) and wavelength interrogation (WI) are two techniques for determining the sensor's potential. The intensity-based measuring approach sometimes referred to as the amplitude interrogation method, uses the variance of loss depth brought on by changes in the analyte refractive index to identify unknown analytes.

$$S_A = -\frac{1}{\alpha(\lambda,n_a)}\frac{\partial\alpha(\lambda,n_a)}{\partial n_a}(RIU^{-1}) \tag{6.5}$$

Here, $\alpha(\lambda,n_a)$ is the confinement loss for a certain sample RI whereas $\partial\alpha(\lambda,n_a)$ signifies disparity in analyte confinement loss between two adjacent refractive indices [121]

Since it evaluates amplitude sensitivity (AS) at a fixed wavelength without requiring spectral manipulation, it is a straightforward approach to put into action. It is, however, sensitive to outside noise, which could affect sensor performance and result in inaccurate analyte detection. This makes the implementation of this method more expensive because additional steps are needed to block outside noise in order to reduce it. In contrast, the wavelength interrogation method additionally allows the determination of the sensor potential by the observation of variations in loss depth resulting from variations in the refractive index of the analyte.

6.3.3 Wavelength Sensitivity (WS):

The wavelength interrogation (spectral-based measurement) method, which takes into account the shift of resonance wavelength, is another way to assess the performance of the sensor. When compared to the AI method, this method typically shows a high-sensitivity response [122] The phase-detection method, often known as the WI method, has the benefit of being cost-efficient. It does have a downside, though, and that is the difficulty of measuring sensitivity [123] The WI method utilizes the following formula to determine a sensor's sensitivity [121]:

$$S_\lambda = \frac{\Delta\lambda_{peak}}{\Delta n_a}(nm/RIU) \tag{6.6}$$

where Δn_a and $\Delta\lambda_{peak}$ represent the difference between two neighboring analytes RI and the contrast in their corresponding resonant wavelengths.

6.3.4 Resolution:

Resolution is a significant parameter in determining the sensor's detection capability. It measures the ability to identify small variations in refractive index (RI). It can take the form of a relation between amplitude ($R(A)$) and wavelength ($R(w)$) [25], [121]:

$$R(A) = \frac{\Delta n_a}{S_A}(RIU) \tag{6.7}$$

$$R(w) = \frac{\Delta n_a \times \Delta\lambda_{min}}{\Delta\lambda_{peak}}(RIU) \tag{6.8}$$

6.3.5 Full Width at Half Maximum (FWHM):

FWHM (Full Width at Half Maximum) is the width of the confinement loss curve when the loss is half of its peak value. It is a measure of the sensing performance of the sensor and reflects how sharp the loss peak is. Sharper loss peaks and higher sensing performance are associated with a smaller FWHM. The sensor's Figure of Merit (FOM) can also be determined using FWHM. As a result, FWHM is an extremely important parameter to use when evaluating a sensor's performance. The procedure for calculating FWHM, which is commonly expressed in terms of nanometers, can be seen in Figure 6.4:
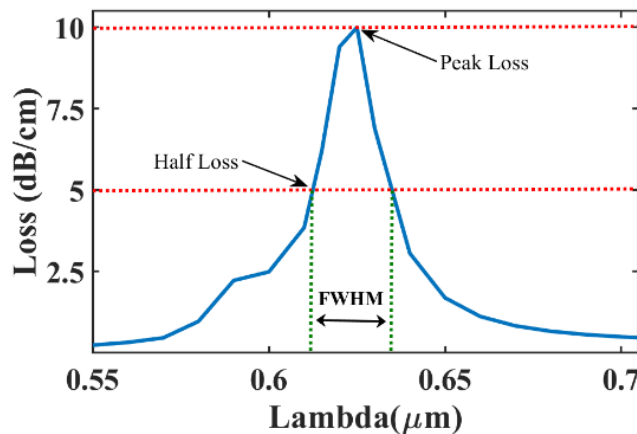
Figure 6.4: Representation of FWHM

6.3.6 Figure of Merit (FOM):

In addition to amplitude sensitivity (AS) and wavelength sensitivity (WS), the figure of merit (FOM) can be utilized for assessing a sensor's effectiveness. The FOM is determined by dividing

the WS (wavelength sensitivity) by the FWHM (Full Width at Half Maximum). When sensor sensitivity increases and FWHM decreases, the FOM value rises, indicating that the sensor is highly efficient. A higher value for WS denotes a more apparent change in resonance wavelength, whereas a lower value for FWHM denotes a more concentrated resonance peak [121]. Because of this, the FOM can be utilized as a stand-in for how well a sensor works in general.

$$FOM = \frac{S_\lambda}{FWHM}(RIU^{-1}) \tag{6.9}$$

6.3.7 Sensor Length:

The length of the sensor corresponding to a specific analyte refractive index (na) can be determined using the peak confinement loss $[\alpha(\lambda, n_a)]$ of that analyte [124].

$$L = \frac{1}{\alpha(\lambda, n_a)}(cm) \tag{6.10}$$

6.3.8 Double Peak Shift Sensitivity for structures having two consecutive resonance peaks:

In certain sensor designs utilizing multiple layers of plasmonic materials, it is possible to observe two distinct peaks for a specific refractive index (RI) being investigated. To quantify the sensitivity of this phenomenon, a specific parameter called double peak shift sensitivity (S_{p-p}) is introduced. It is defined as the difference between the peak-to-peak distances of the two resonance wavelengths (RW) and is related to the analyte RI [115]:

$$S_{p-p} = \frac{(\lambda_{p2} - \lambda_{p1})_{n_b} - (\lambda_{p2} - \lambda_{p1})_{n_a}}{n_b - n_a} \times 10^3 (nm/RIU) \tag{6.11}$$

Or,

$$S_{p-p} = \frac{(\lambda_{p2,n_b} - \lambda_{p2,n_a}) - (\lambda_{p1,n_b} - \lambda_{p1,n_a})}{n_b - n_a} \times 10^3 (nm/RIU) \tag{6.12}$$

where, S_{p-p} stands for DPSS, whereas λ_{p1,n_b} and λ_{p1,n_a} represent the primary resonance wavelengths, and λ_{p2,n_b} and λ_{p1,n_a} describe the secondary resonance wavelengths of refractive indices n_b and n_a, respectively.

6.4 Conclusion:

Throughout the preceding chapters, we have acquired knowledge about the necessary materials of an SPR-based PCF sensor and the performance parameters used to evaluate its efficiency. In the following chapters, we'll utilize the equations and performance characteristics of these materials to characterize and evaluate our proposed sensor construction.

CHAPTER – 7

ANALYSIS OF AN LSPR BASED PCF SENSOR WITH SILVER-GZO COMBINATION

7.1 Introduction:

Here, we employ a novel plasmonic material configuration in which Silver (Ag) and Ga-doped ZnO (GZO) work together to detect analytes. The sensor's detecting capabilities are improved by the presence of two peaks with the same Refractive Index (RI). The first peak is caused by GZO, and the second peak is caused by Ag. In terms of y-polarization, a DPSS of 27,341.5 nm/RIU is found which is the highest number reported to date. The amplitude sensitivity (AS) of the sensor is 875.72 RIU^{-1}, and the wavelength sensitivity (WS) is 27,360 nm/RIU. The sensor also exhibits a high amplitude resolution of 1.496×10^{-5} and a wavelength resolution of 6.032×10^{-6}. A linearity of R2=0.9973 and a FOM of 243.4 RIU^{-1} can be seen from the sensor. After conducting a thorough fabrication tolerance analysis, we find that both the confinement loss and the resonant wavelength shift are unaffected by a ± 10-tolerance limit. A wide range of RI up to 1.27 to 1.41 is investigated, which broadens its potential applicability to the detection of pharmaceuticals and other compounds. In addition, the sensing parameters in RIs that were not numerically analyzed have been sought through the use of machine learning regression techniques in this study. No relevant work was found which used regression algorithms to analyze the performance parameters were found to the best of our knowledge. As input, the RI of the analyte is given to the algorithm while the output target variables are the shift in the GZO and Ag peak resonant wavelengths in two consecutive RIs respectively. The accuracy of the Random Forest Regressor was determined to be 90.176%, whereas that of the K-Nearest Neighbors Regressor was 95.54%. This research presents a new approach to assessing sensor performance metrics, which not only facilitates quicker and more accurate predictions but also saves considerable amounts of time. Sensor performance may be better understood with this new approach, which will lead to improvements across disciplines and pave the way for more effective and dependable sensing technology.

7.2 Sensor Architecture and Materials for Enhanced Performance:

(a)   (b)
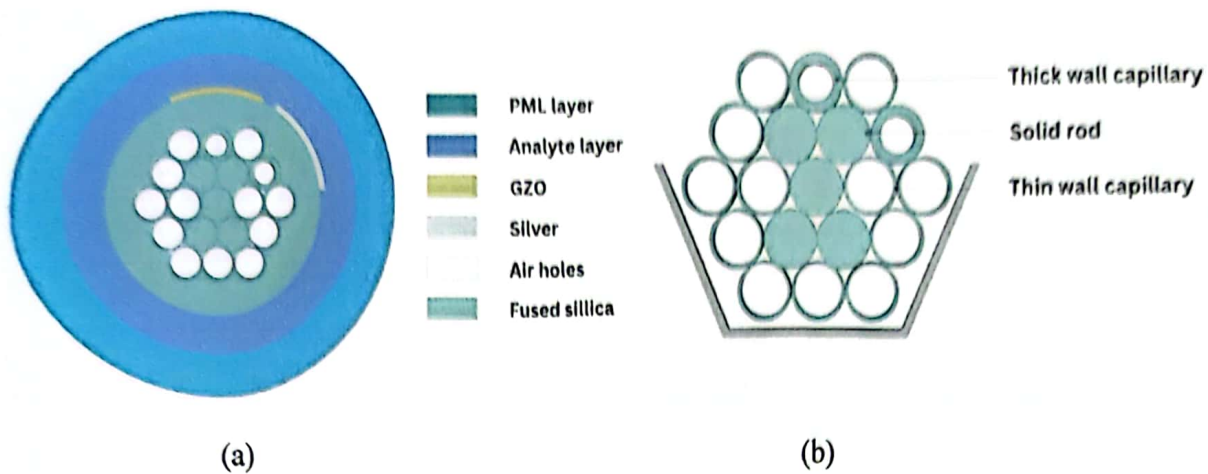
Figure 7.1: (a) Configuration of the PCF sensor, showcasing a two-dimensional representation of the distribution of air holes, plasmonic layers, analyte layer, and the PML layer (b) PCF sensor fabrication using a layered preform structure

Figure 7.1 shows a two-dimensional model of the sensor created for this study. COMSOL Multiphysics 5.6 was used for the sensor's design, simulation, and optimization. A Perfectly Matched Layer (PML) and an analyte layer follow the circular cladding structure made of fused silica to aid in external sensing. In the configuration depicted in Figure 7.1, two plasmonic materials, silver and GZO, are arranged along the central PML surface. Since silver has a greater resonance peak, it is favored, but GZO is preferred due to its inexpensive cost and high carrier concentration. Since using two distinct plasmonic materials (such as gold and silver) would drive up production costs, combining GZO and silver is a cost-effective alternative.

The hexagonal cladding is punctured with fourteen air holes, twelve with a greater radius r1 μm and two smaller air holes with a radius of r2 μm. The hexagonal shape is formed by ten bigger air holes and two smaller air holes, with the other two larger air holes located centrally. Air hole placement in the sensor's design has to optimize light confinement in the core while reducing loss. Again, there has to be a good route for energy to get from the center to the surface plasmon waves. Smaller air holes, oriented toward the two plasmonic layers, functioned as the pavement for energy transmission. The bigger holes performed the earlier goal of dense light containment while minimizing the confinement loss (CL).

7.3 Optimization of Structural Parameters using the DPSS Interrogation Method:

In the past, WS and AS have been used among others to optimize structural characteristics. In this work, we use the DPSS parameter to improve the sensor specifications. To achieve maximum sensitivity, the plasmonic layers' thickness and the radii of the bigger and smaller air holes along the y-polarization are optimized using the finite element method (FEM). At first, both the GZO and silver plasmonic layers were 30 nm thick, and the air holes' radii were 0.75 and 0.25 μmeters, respectively. The width of the PML and analyte layer was initially set at 1 μm and 2μm respectively.

7.3.1 Thickness of Ag and GZO layer:

The DPSS of the fiber was analyzed for refractive indices of 1.37 and 1.38. At first, the GZO layer was optimized and then the Ag layer. With respect to the GZO layer, the sensor's DPSS improved along with decreasing layer thickness, reaching a maximum of 3581 nm/RIU at a thickness of just 1 nm. As a result, the ideal thickness of the GZO layer was determined to be 1 nm. The CL of the fiber is shown in Figure 7.2(a), and the trend of the change of the DPSS with the alteration of the GZO layer width is shown in Figure 7.2(b).

(a)

(b)

(c)

(d)

42
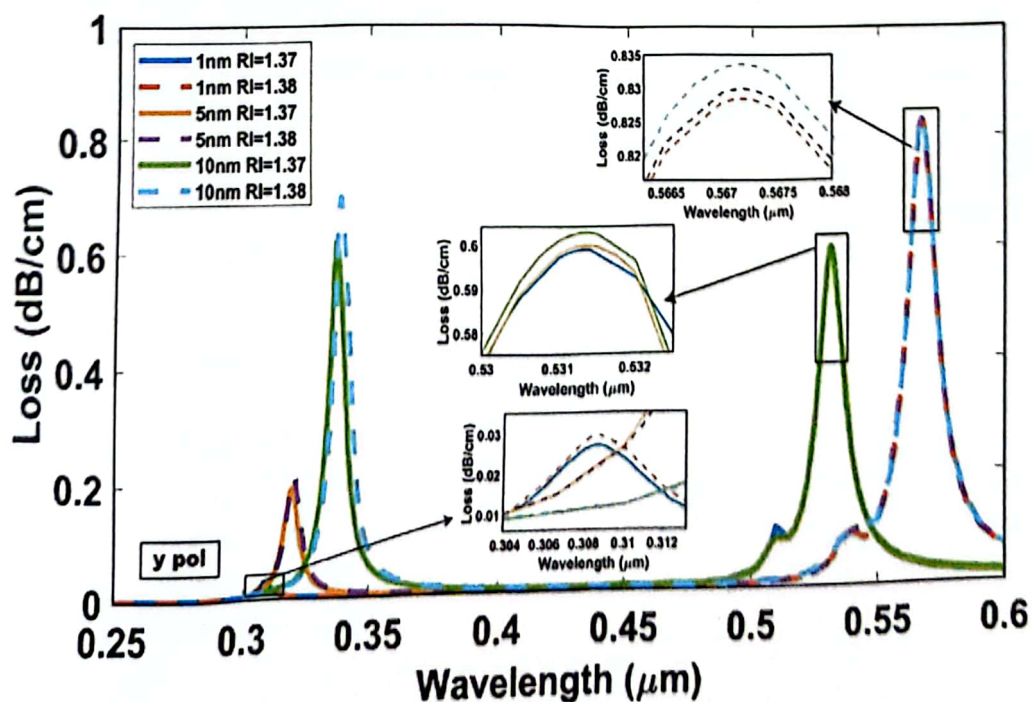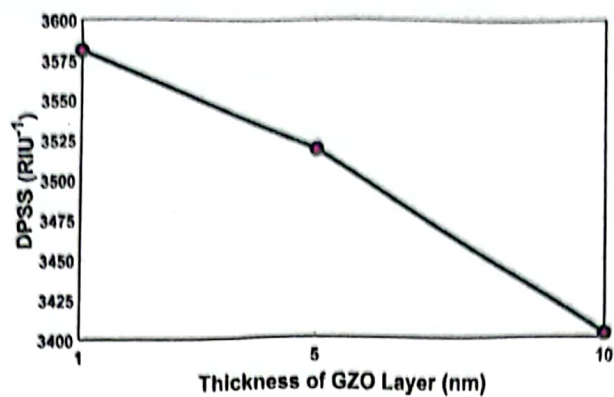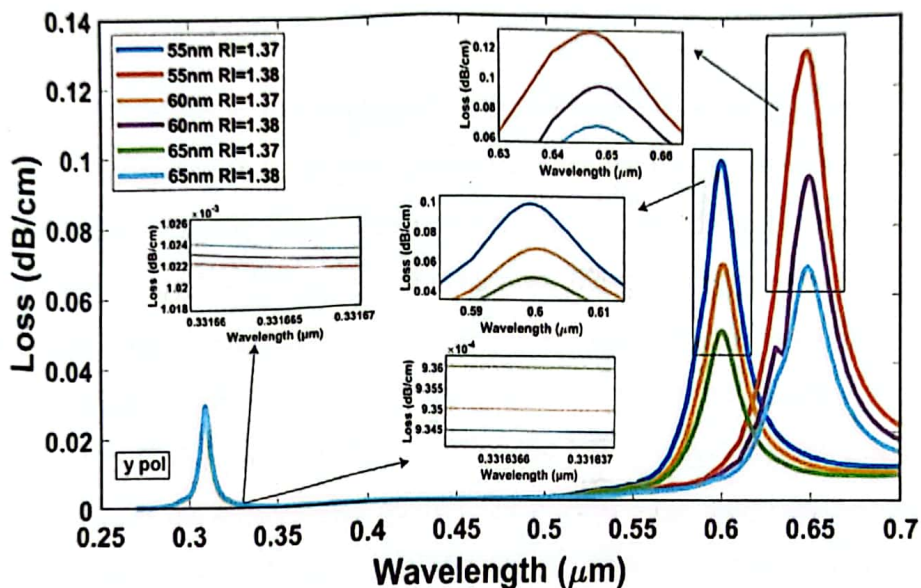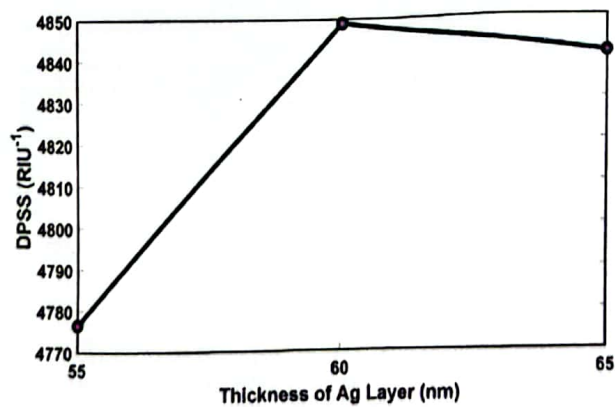
Figure 7.2: Consequence of varying the GZO layer thickness on (a) CL and (b) DPSS and Ag layer thickness on (c) CL and (d) DPSS at an RI 1.37 and 1.38 respectively

The Ag layer was honed in the same way. As the Ag layer thickness was raised, the DPSS rose until the thickness was 60 nm. Figures 7.2(c) and (d) depict the CL vs. wavelength and the variation in DPSS with the modification of the Ag layer width, respectively. A high value of 4849 nm/RIU was achieved at a width of 60 nm, and the DPSS indicated minimal confinement losses of 0.0269 dB/cm and 0.0685 dB/cm at RI=1.37. If the width of the Ag layer is increased further, the damping of light rises, reducing the DPSS of the fiber. This is because the light rays have a more difficult time penetrating the thick layer.

7.3.2 Variation in Air Hole Radii:

After optimizing the plasmonic layer thickness, the air hole radii were then tuned to find out the optimum DPSS of the sensor along y-polarization. When the bigger air hole radius was reduced to 0.7 m, the sensor's CL rose from 0.0686 dB/cm to 0.0863 dB/cm at the resonance wavelength reaching 0.6 μm but declined to 0.0532 dB/cm when the radius was expanded to 0.8 μm. The bigger air hole (r1) performed better with the initial set radii of 0.75 μm as altering the radii only resulted in lowering the DPSS. At r2=0.2 μm, with a loss value of 0.11798 dB/cm, the sensor's DPSS increased to 4851.5 nm/RIU. The fact that the loss is still rather little despite the slight increase demonstrates the sensor's high quality. The results of the study demonstrate that altering the radius of the air holes on the neighboring sides decreases surface plasma formation and, by extension, the sensitivity and SPR impact [41].
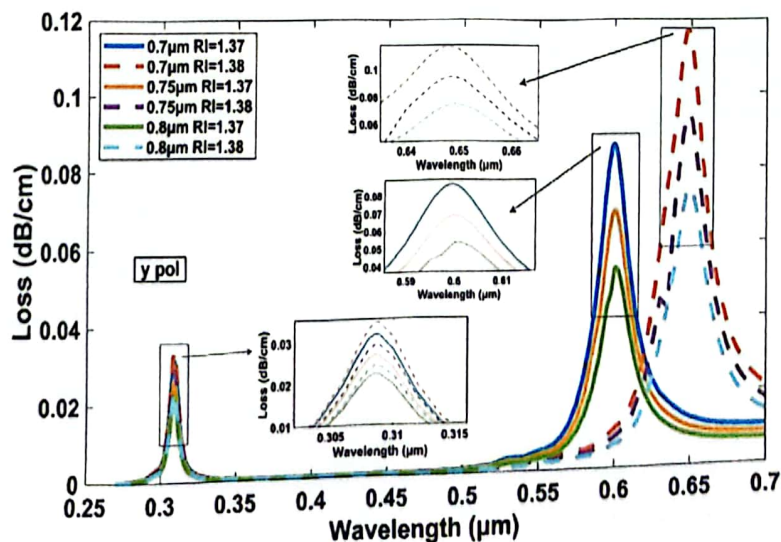
(a)
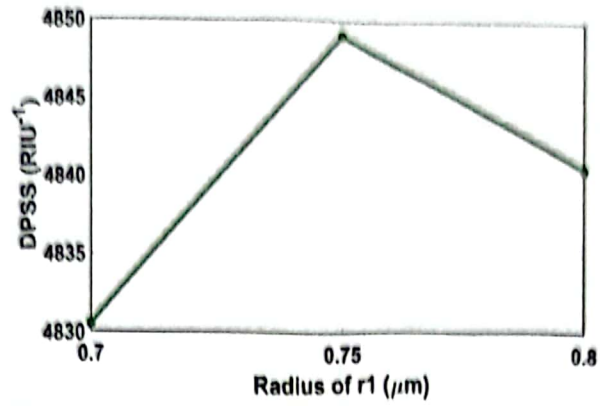
(b)
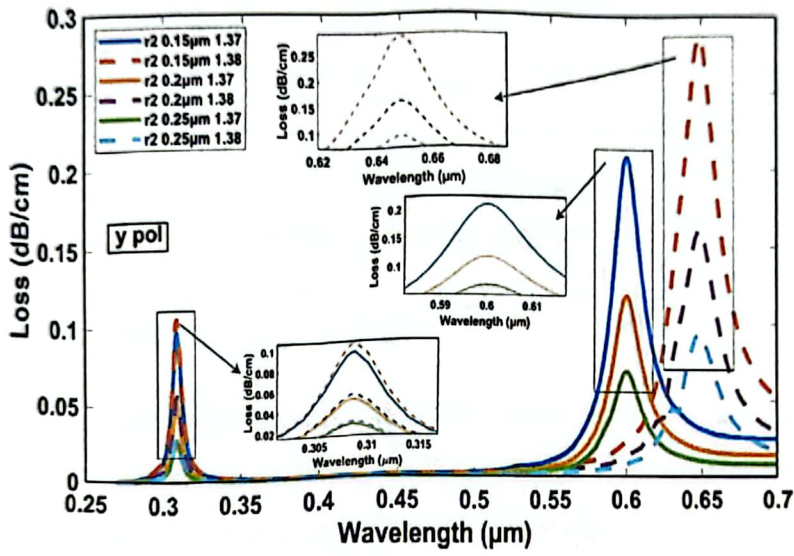
(c)
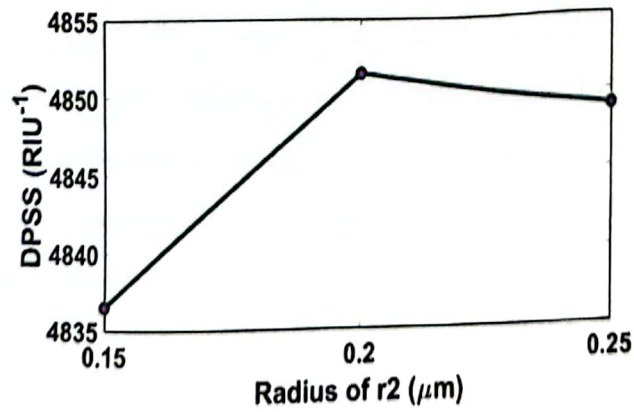
(d)

Figure 7.3: Consequence of varying the larger air hole radii on (a) CL and (b) DPSS and smaller air hole radii on (c) CL and (d) DPSS at an RI 1.37 and 1.38 respectively

Previous research in this area suggests that the sensor's sensing characteristics are mostly unaffected by the analyte and PML layer's optimization. There is no change in the sensor's WS, and the AS fluctuates just a little. Since the DPSS is just a modified version of the WS, we did not alter the PML and analyte layer.

TABLE 7.1: INITIAL AND FINAL PARAMETER VALUES BEFORE AND AFTER INVESTIGATION:

Structural Parameter Name	Initial Width	Final Width
GZO layer width	30 nm	1 nm
Ag layer width	30 nm	60 nm
Larger air hole radius	0.75 µm	0.75 µm
Smaller air hole radius	0.25 µm	0.2 µm

7.4 Unique Characteristics of the Sensor's Quality:

7.4.1 Double Resonance:

When the evanescent field frequency coincides with the frequency at which the electrons in the sensor's plasmonic material are vibrating, surface plasmon resonance is established. Light confinement within the fiber is maximized when the sensor achieves resonance by matching the effective indices of the core guided mode and the SPP mode at a given wavelength. A confinement peak loss may be seen at the same time as resonance. The sensor's dual plasmonic material composition (Ag and GZO) generates a bifurcated evanescent field that gives rise to two separate SPP modes. SPP modes interact with the core mode across a broad frequency range due to the special properties of Ag and GZO. This means that there are two unique peaks for each polarization, and that there are two distinct resonance wavelengths where they can be inhibited under phase-matching circumstances.
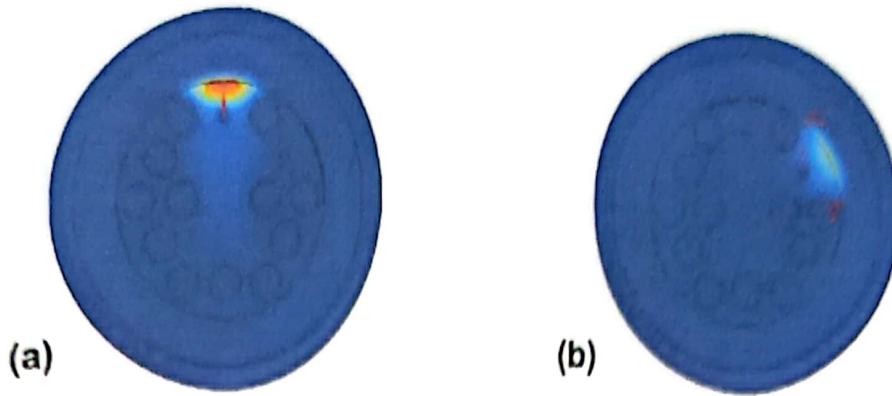
Figure 7.4: For y-pol, at an RI 1.37, SPP mode along (a) GZO layer (b) Ag layer at the resonant wavelengths of each loss peak

Figure 7.4 shows the several SPP modes that the sensor exhibits within the same RI. Figure 7.4(a) shows the SPP mode along the GZO layer at the first resonant wavelength, whereas Figure 7.4(b) displays the SPP mode along the Ag layer at the second resonant wavelength. Therefore, the first peak in the confinement loss vs. wavelength curve of the sensor is due to the GZO layer, while the second peak is due to the Ag layer, both of which were unexplained in any previous studies displaying dual peaks within the same RI.

7.4.2 Analysis of Performance Parameters:

- **Double Peak Shift Sensitivity:**

Using equation (6.11) or (6.12), the DPSS of the sensor was calculated. The sensor portrays a maximum DPSS of 16,571 nm/RIU for x-polarization at an RI of 1.40 and 27,341.5 nm/RIU at an RI 1.41 for y-polarization.
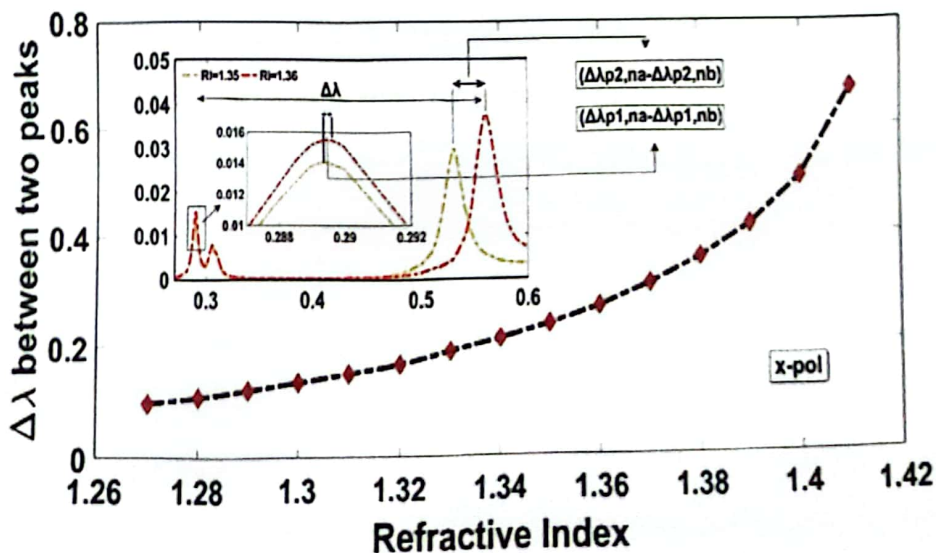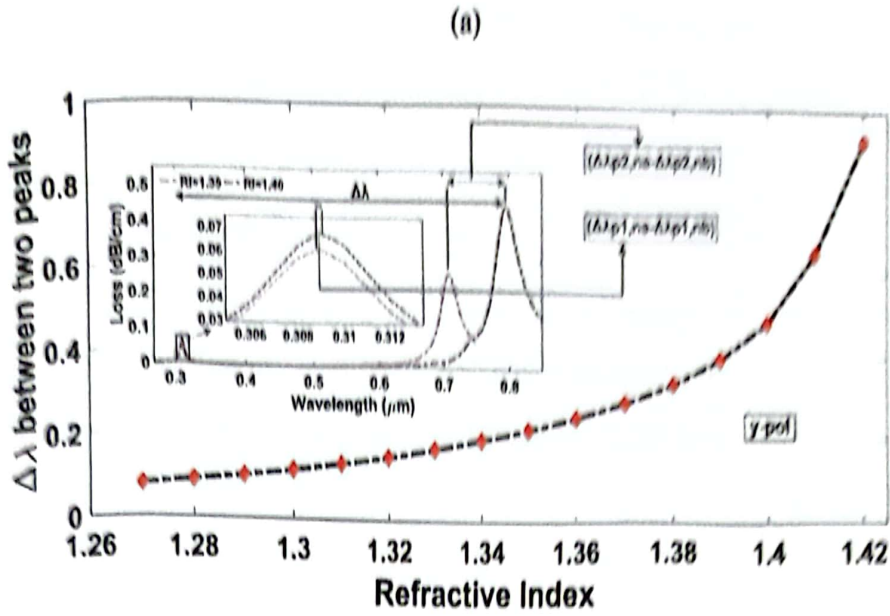
(b)

Figure 7.5: Difference in RW for the two peaks along (a) x-pol (b) y-pol
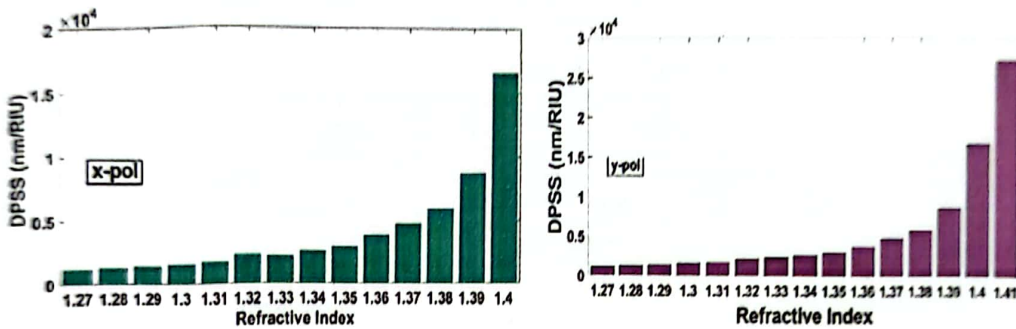
| (a) | (b) |

Figure 7.6: Increment in DPSS with RI (a) x-pol (b) y-pol

Since the two peaks experience different levels of loss, the peak transfer of energy from the core mode to the SPP mode varies at different resonant wavelengths (RW) as a result of light scattering. The sensor upholds the highest difference of 0.575 dB/cm for the two loss peaks for x-pol and that of 7.515 dB/cm for y-pol, which can help in precise analyte recognition with very minimal loss.

- **High Spectral Sensitivity (WS):**

Using equation (6.6), a high WS of 16,578 nm/RIU is achieved by changing the RI from 1.40 to 1.41, which causes the sensor's resonant wavelength to shift from 795 nm along x-polarization to

961 nm. The resonant wavelength for y-polarization moves from 963 nm to 1237 nm when the RI of the analyte changes from 1.41 to 1.42. This corresponds to a maximum WS of 27,360 nm/RIU.

- **Maximum Amplitude Sensitivity (AS):**

With a RI of 1.38, using equation (6.5), the developed sensor has an AS of 875.716 RIU^{-1} along y-pol and 668.238 RIU^{-1} along x-pol. Since additional increases in RI lead to a degradation in the AS curve and overall amplitude sensitivity, our studies of AS have been restricted to the RI 1.39 level. When compared to the AS produced in prior research using either Ag or GZO as plasmonic materials [107]–[109], [111], [117], [118], the result attained here is really impressive.
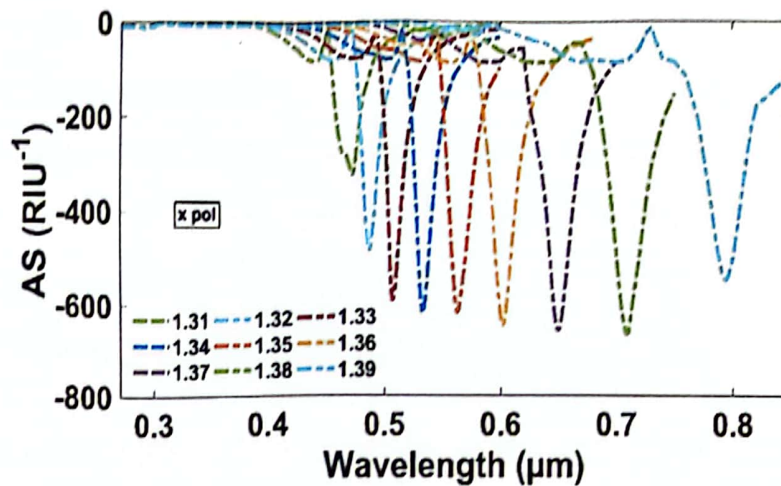
(a)
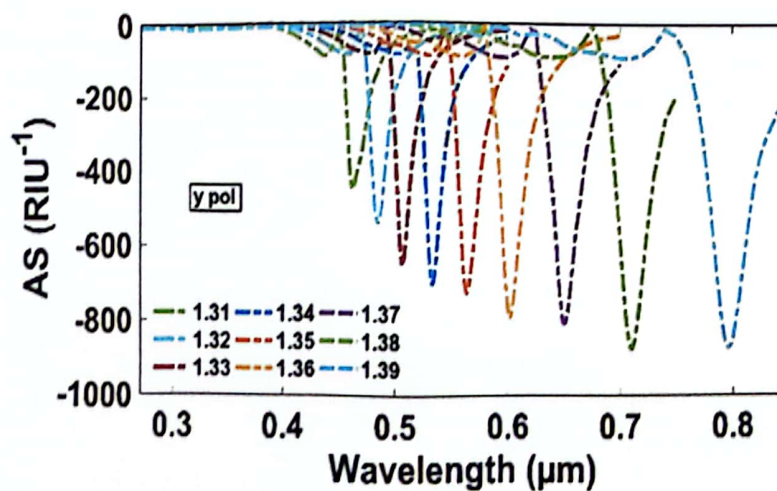
(b)

Figure 7.7: AS vs wavelength curve for an RI range of 1.31 – 1.39 (a) x-pol (b) y-pol

- **Figure of Merit (FOM):**

Using equation (6.9), the recommended sensor displays an FOM of 243.44 RIU^{-1} along x-polarization and 212.258 RIU^{-1} along y-polarization.

- **Sensor Length:**

For x-polarization, the longest possible sensor length is discovered to be 136.37 cm, while for y-polarization, the longest is 65.39 cm which we found from equation (6.10). Therefore, the suggested sensor provides an acceptable compromise between sensitivity and ease of fabrication.

- **High Sensor Resolution:**

The developed sensor has a reported amplitude resolution of 1.4961×10^{-5} along x-pol and 1.142×10^{-5} along y-pol using equation (6.7), as well as 6.032×10^{-6} along x-pol and 3.655×10^{-6} along y-pol using equation (6.8). Therefore, RI changes on the order of 10^{-6} can be detected by the sensor using wavelength interrogation method and 10^{-5} using amplitude interrogation method.

7.4.3 Versatile Analyte Detection Capabilities:

One of the sensor's main selling points is its ability to detect analytes with a wide range of refractive indices, from 1.27 to 1.40 for x-pol within a scale of 270 nm to 1100 nm, and from 1.27 to 1.41 for y-pol within a spectrum range of of 270 nm to 1300 nm.

(a)

(b)
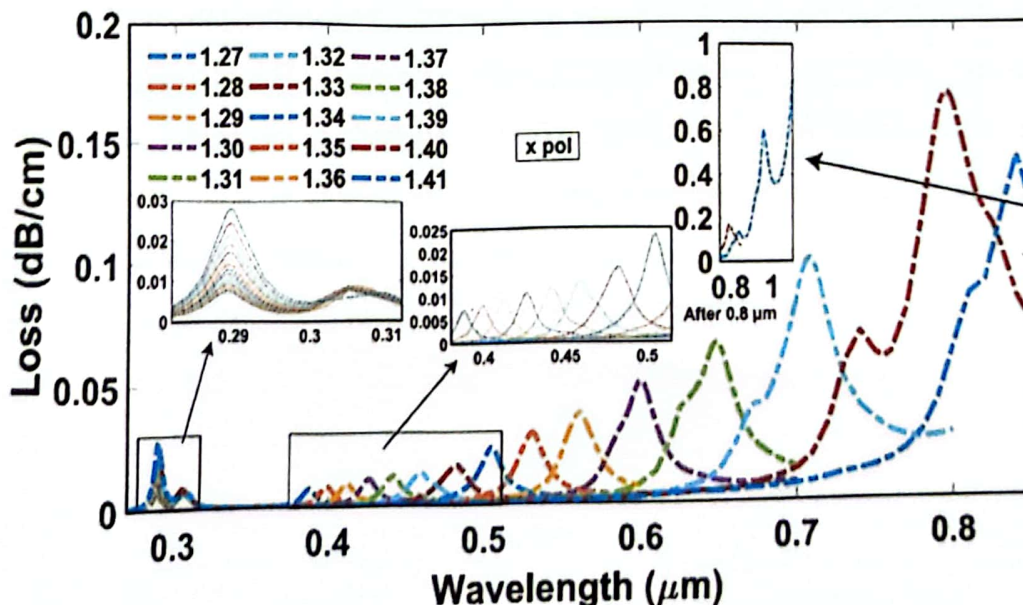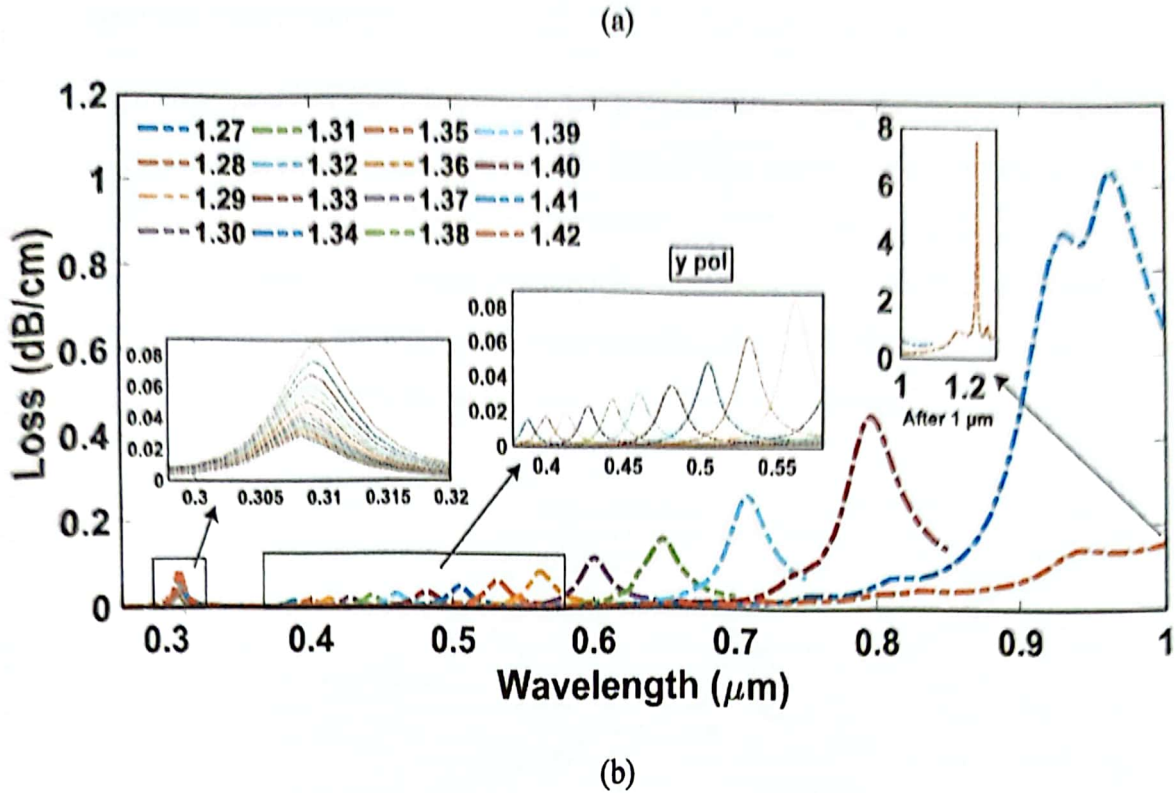
Figure 7.8: CL vs. wavelength curve for an RI range of (a) 1.27-1.41 for x pol and (b) 1.27-1.42 for y-pol

Figure 7.8 shows that the two different plasmonic materials utilized cause a red shift in the CL vs. wavelength curve when the refractive index is raised. Figure 7.8 shows that the sensor's essential and appealing characteristic, the low confinement loss, remains true even at higher refractive indices: 7 dB/cm at 1.42 RI for y-pol and 0.6 dB/cm at 1.41 RI for x-pol. Once more, the sensor exhibits two resonant peaks for each RI, which will allow for significantly more exact detection of analytes. If the RI of the analyte is steadily raised, it will eventually approach that of the cladding zone submerged in fused silica. When the core and cladding are coupled optimally, the cladding allows the most evanescent light to pass through. When the propagation factor is lowered by decreasing the refractive index, the core and SPP modes are more likely to coincide at longer wavelengths. However, beginning with refractive indices of 1.37 for x-pol and 1.40 for y-pol, the curve undergoes a minor distortion. In other words, y-pol is where the sensor functions most efficiently.

7.4.4 Sensor Calibration:

A high linearity between the refractive index of the analyte and the resonant wavelength is indicative of a high-quality, straightforwardly calibratable sensor. Linear sensor x-polarization fitting follows the equation y=3.384x-3.981 with R^2=0.8533, as shown in Figure 7.9 (a). When the same curve is used to fit a fourth-order polynomial equation, R^2 =0.9973 is obtained, which is close to 1. Similarly, a 4th order polynomial equation with R^2=0.9965 may be used to fit the y-polarization curve. As a result, the sensor guarantees top-notch operation.
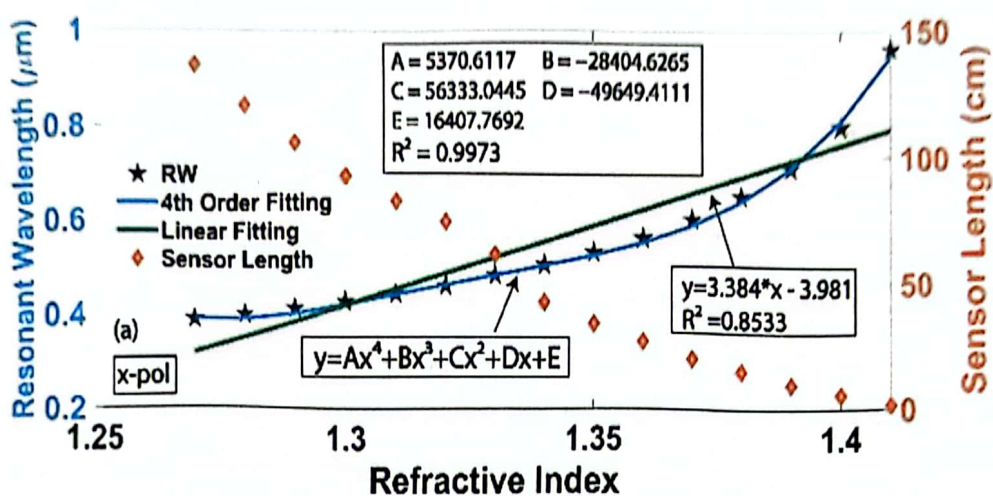
(a)
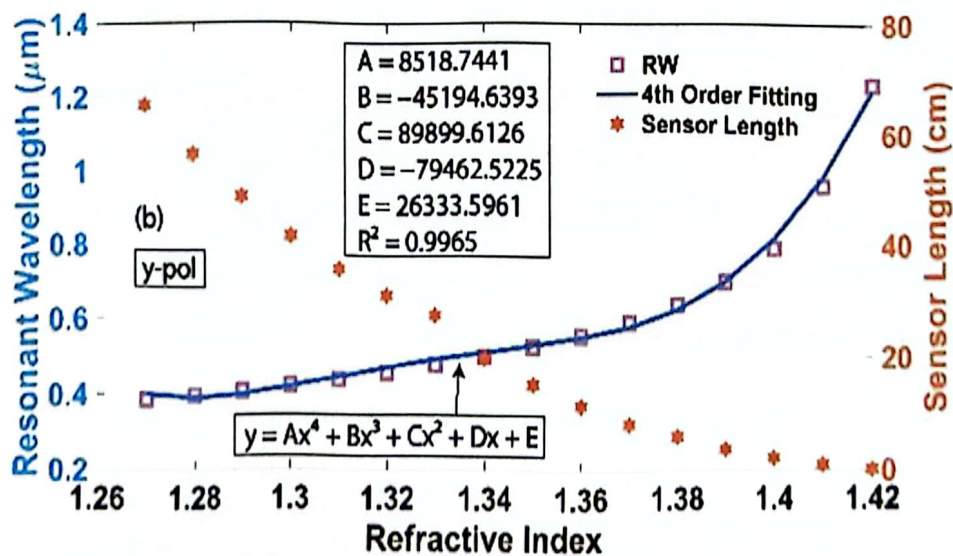
(b)

Figure 7.9: Polynomial fitting curve for the Ag peak along (a) x-pol and (b) y-pol

7.5 Result Verification using Machine Learning Algorithms:

At the past, sensor performance at refractive indices where it had not been tested or studied was determined by curve fitting and extrapolation methods. However, given the rapid development of machine learning, this study investigates the use of a few regression techniques that may be used to forecast the sensor's performance characteristics.

Machine learning (ML) algorithms are data-driven software routines that can function independently of clear instructions [125]. These algorithms use statistical approaches to find patterns in data and then make inferences or judgments based on those patterns. Predicting discrete values, regression algorithms use ML methods [126]. Recent years have seen the optimization of PCF structures using deep learning methods including genetic algorithms, artificial neural networks (ANN), and genetic adversarial networks (GAN) [127]–[130]. However, the use of machine learning algorithms to forecast the numerical values of sensitivity or the location of resonant peaks by developing a link among specific factors using the data acquired from the traditional simulations of PCF sensors has not yet been explored. In order to anticipate the sensitivity and resonance peaks, this research proposes a unique technique that employs a number of machine learning regression methods. This method may be used in conjunction with extrapolation and curve fitting techniques to gain a rough idea of where the peak could be and the sensitivity parameters, which can greatly reduce the amount of time and effort spent on the project.

Table 7.3 shows the accuracy scores achieved by running the algorithms on the dataset presented in table 7.2. Here, we use as input features the refractive indices of the analyte and as output variables the sensing parameter, double peak shift sensitivity, and the shift in the GZO and Ag peak resonant wavelengths in two successive RIs. Therefore, the resonant wavelength shift between two successive RIs and the DPSS may be roughly estimated using just the RI as input.

TABLE 7.2: MACHINE LEARNING REGRESSION ALGORITHM DATASET USED

Refractive Index	Difference of Ag peak (μm)	Difference of GZO peak (μm)	DPSS (nm/RIU)
1.27	0.01175	0.000025	1172.5
1.28	0.0129	0.000055	1245
1.29	0.01423	0.00003	1420

1.3	0.015645	0.00005	1559.5
1.31	0.017325	0.000035	1729
1.32	0.02141	0.000065	2134.5
1.33	0.0236	0.000065	2353.5
1.34	0.02655	0.000055	2649.5
1.35	0.030355	0.00007	3028.5
1.36	0.038185	0.000085	3810
1.37	0.0486	0.000085	4851.5
1.38	0.05987	0.000115	5975.5
1.39	0.08726	0.00013	8713
1.40	0.16757	0.000155	16741.5
1.41	0.2736	0.000185	27341.5

TABLE-7.3: OBTAINED RESULTS WITH REGRESSION ALGORITHMS

ALGORITHMS	ACCURACY
RFR	90.176%
LR	86.826%
K-NR	95.54%

The algorithms have been run using Google Colab. Table-I's dataset has been partitioned into a testing and training phase. Seventy-five percent of the data was used to train the models, and the remaining 25 percent was utilized to evaluate the effectiveness of the method. The accuracy of three different regression algorithms in predicting the three output target variables was then evaluated by running them on the dataset: the Random Forest Regressor (RFR), the Linear Regressor (LR), and the K-Neighbors Regressor (K-NR). Accuracy tests indicated that the Random Forest Regressor and the K-Nearest Neighbors Regressor algorithms performed at 90.176% and 95.54%, respectively, whereas the Linear Regressor performed at 86.826%. As a result, it is clear that ML algorithms are also a viable option for estimating the sensor's performance in RIs that have not been subjected to testing. The sensor's other parameters, such as its WS, AS, FOM, etc., may be calculated in the same way by making a data table like table-I and applying the same kinds of algorithms.

Using the results obtained from table-II, the algorithms were used to predict the sensitivity of several chemicals when used as analytes. The results obtained are tabulated below in table-7.4:

TABLE-7.4: PREDICTED THE PERFORMANCE OF THE SENSOR IN DETECTING VARIOUS CHEMICALS

Algorithm	Ag Peak Difference (μm)	GZO Peak Difference (μm)	DPSS (nm/RIU)
Methanol (RI=1.329)			
RFR	0.02376	0.000063	2369.64
LR	0.04232	0.0000704	4220.43
K-NR	0.026105	0.0000633	2641.67
Ethanol (RI=1.358)			
RFR	0.03661	0.0000808	3653.305
LR	0.075055	0.00007033	7494.096
K-NR	0.03905	0.00008	3896.667
Acetic Acid (RI=1.372)			
RFR	0.05013	0.0000916	5003.775
LR	0.090856	0.00010888	9074.4888
K-NR	0.048885	0.000095	4879
Tetrahydrofuran (RI=1.408)			
RFR	0.203666	0.0001634	20,350.25
LR	0.131486	0.00014116	13,138.355
K-NR	0.140243	0.0001433	14,010
n-Decane (RI=1.412)			
RFR	0.203666	0.0001634	20,350.25
LR	0.136	0.0001447	13,589.896
K-NR	0.14024	0.0001433	14,010

Thus, from this analysis, we can safely say that it is feasible to predict the sensor's response to unknown analytes using the previously obtained data by employing regression methods. K-

Neighbors Regressor and Random Forest Regressor were shown to have the best accuracy rates, suggesting that estimates made using these two methods are more reliable. This analytical method results in significant time and energy savings.

7.6 Comparison with Related Works:

Table-7.5 shows a study compared to other studies that have been reported in the literature. Based on these findings, it is clear that the proposed sensor achieves superior results when employing both Ag and GZO as plasmonic materials simultaneously for detecting analytes. To the best of our knowledge, this is the first work to investigate the sensor's performance across a broad range of RIs utilizing silver as a plasmonic material. Materials responsible for the two plasmonic peaks are also explained in this paper, something that has not been done previously. In addition, this study proposes using ML algorithms to predict the sensor's output in RIs that have not been tested before, demonstrating the originality and distinctiveness of the work.

TABLE-7.5: COMPARATIVE ANALYSIS WITH RELATED WORKS IN THIS FIELD

Ref.	Materials	RI Range	AS (RIU^{-1})	WS (nm/ RIU)	Resolution		FOM	DPSS (nm/ RIU)
					Wavelength	Amplitude		
[117]	Ag	1.34-1.37	-	5000	-	-	-	-
[108]	Ag	1.33-1.37	300	4200	2.38×10^{-5}	3.33×10^{-5}	-	-
[107]	Ag	1.33-1.42	-	16700	5.99×10^{-6}	-	-	-
[109]	Ag	1.25-1.30	-	1932.09	3×10^{-5}	-	-	-
[111]	GZO	1.24-1.40	135.82	17000	5.88×10^{-6}	7.36×10^{-6}	45.94	
[112]	Ag / Graphene	1.33-1.41	-	12600	7.94×10^{-6}	-	-	-
[114]	ITO+ZnO	1.30-1.38	-	10000	2×10^{-5}	-	-	-
[115]	AZO+Au	1.27-1.42	8485.2	46300	2.16×10^{-6}	1.18×10^{-6}	-	16500
[127]	Ag / Graphene	1.46-1.49	418	3000	3.33×10^{-5}	2.4×10^{-5}	-	-
[131]	Ag / Graphene	1.33-1.35	72.47	2520	3.97×10^{-5}	-	-	-

[113]	Ag / Graphene	1.33-1.37	216	3700	2.7×10^5	4.6×10^5	-	-
Our work	GZO+Ag	1.27-1.41	875.72	27360	1.142×10^5	3.65×10^6	243.4	27341.5

7.7 Fabrication Steps and Fabrication Tolerance Analysis:

The fabrication methods must also be shown to ensure the sensor can be used in practice. sensors. Fabrication is best approached simply rather than intricately, taking into account factors like complexity and cost [132]. Figure 7.10 depicts a possible manufacturing process. The primary components are capillaries of two sorts and solid rods. The suggested sensor's core and cladding region may be built using the stack and draw manufacturing technique [133]. This method allows for a great deal of design flexibility due to the fact that the core size, shape, and index profile may all be changed across the board in the cladding.

Capillaries and solid rods are placed to mimic the air hole pattern of the proposed sensor to create the structure. Then, the cane, which serves as a steppingstone, must be drawn until accurate dimensions are acquired. Two plasmonic films, Ag and GZO, are proposed for use in the sensor. Two-stage photolithography [134] is required to do this. The initial plasmonic layer can be created around the drawn cane using the chemical vapor deposition (CVD) approach, in which a coating is produced on a heated substrate by thermally induced processes at the substrate surface [135]. The first plasmonic layer is then generated by masking and etching the region specified in the design. The second plasmonic layer may be generated in the same way. One pump will allow analytes to reach the detecting layer, while the other will prevent their access [124].

1

Solid rod

Thick wall capillary

Thin wall capillary

2

Stacking

3

Cane

4

Drawing

5

CVD of plasmonic layer 1

6

Masking and etching of plasmonic layer 1

7

Plasmonic layer 1

8

CVD of plasmonic layer 2

9

Masking and etching of plasmonic layer 2

10

Plasmonic layer 2

Plasmonic layer 1
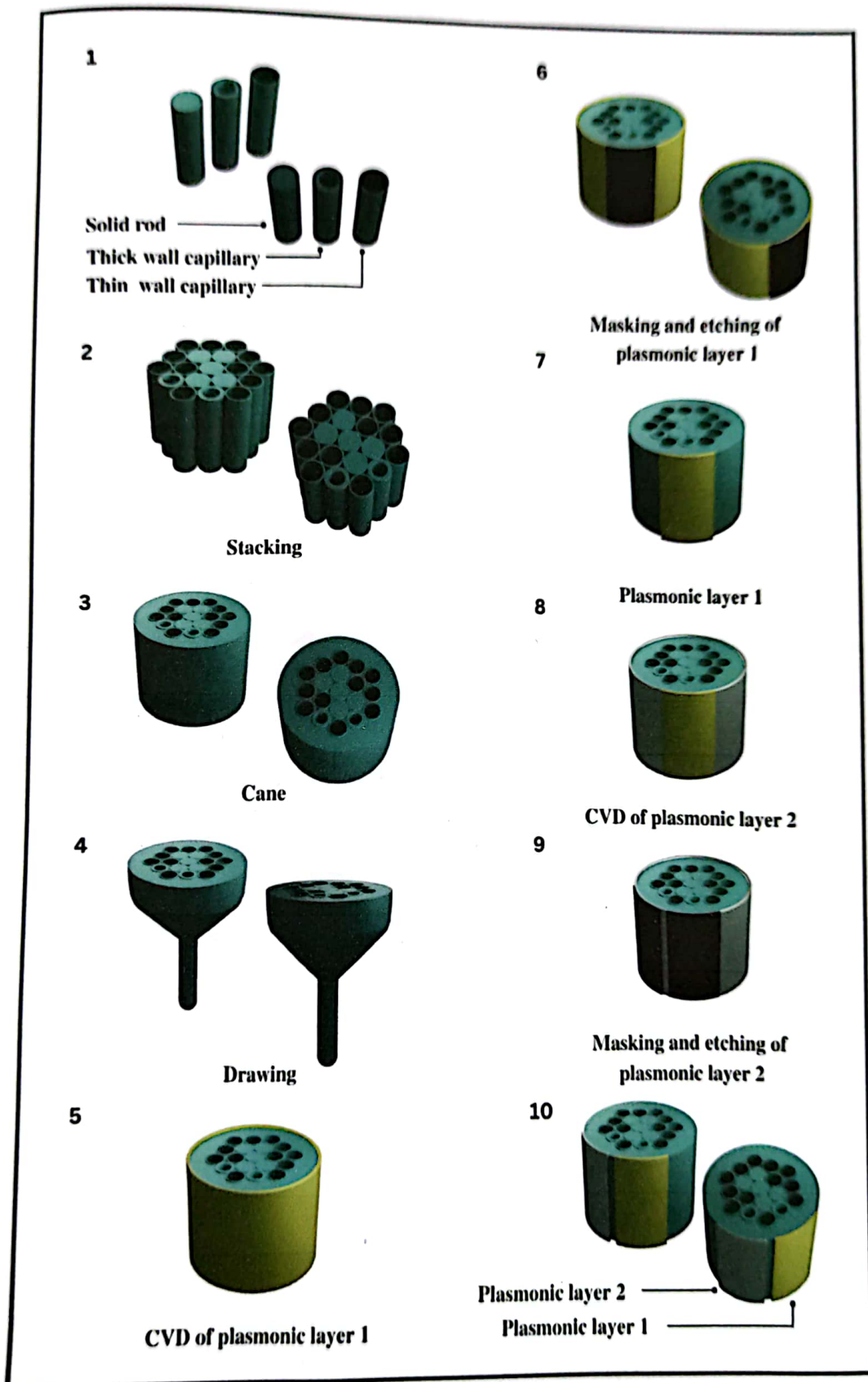
Figure 7.10: Probable steps of fabrication of the proffered sensor

However, it is not possible to manufacture the sensor to the specified size due to the constraints of the fabrication procedures. There is always found to be a fluctuation of ±1% or ±2% in the proportions in these well-established regular procedures. Therefore, fabrication tolerance analysis is carried out to determine the sensor's potential adaptability. Figure 7.11 and table-7.6 show that the CL of the sensor is not noticeably affected by a ±5% or ±10% difference. When the radii of the two air holes are made smaller, the sensor's CL rises somewhat, and when they are made larger, it falls. It follows that the sensor is quite adaptable, since it will not show any major change even if the dimensions alter by a margin of ±10%.
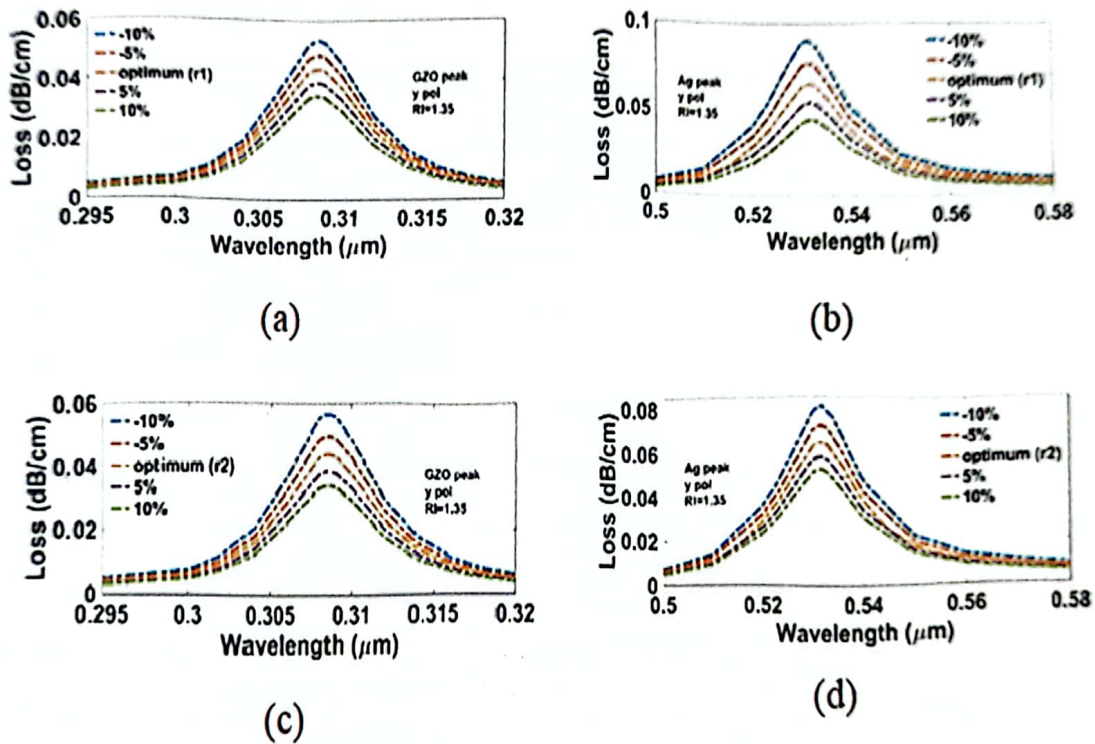
Figure 7.11: CL curve at analyte RI 1.35, showing 5% and 10% variation in r_1 on (a) GZO peak (b) Ag peak (c) and in r_2 on (c) GZO peak (d) Ag peak

TABLE-7.6: CONSEQUENCE OF VARYING THE AIR HOLE RADII ON THE CL OF THE SENSOR

Variation in r_1			Variation in r_2		
	CL (dB/cm)			CL (dB/cm)	
Change in dimension	GZO peak	Ag peak	Change in dimension	GZO peak	Ag peak
-10%	0.0535	0.0901	-10%	0.0566	0.0808
-5%	0.0486	0.0768	-5%	0.0498	0.0723
0	0.0439	0.0648	0	0.0439	0.0648
5%	0.0393	0.0539	5%	0.0387	0.0581
10%	0.0349	0.0439	10%	0.0341	0.0521

7.8 Conclusion:

The sensor's novel structural formulation makes it useful for detecting pharmaceuticals, chemicals, and medical procedures throughout a wide refraction index range (from 1.27 to 1.41). The sensor's maximum DPSS along y-polarization is 27,341.5 nm/RIU at a RI of 1.41, while its maximum DPSS along x-polarization is 16,571 nm/RIU at a RI of 1.40. The sensor's dual peaks, which result from the novel combination of plasmonic materials, allow for highly sensitive detection of analytes. Once again, the y-polarization indicates a high WS of 27,360 nm/RIU and an AS of 875.716 RIU^{-1}. The sensor's fabrication is highly versatile, allowing for a $\pm 10\%$ tolerance range without noticeably altering the loss of confinement and shift in resonant wavelength. In addition to portraying an FOM of 243.4 RIU^{-1}, the sensor is capable of a maximum amplitude resolution of 1.49 x 10^{-5} and a maximum wavelength resolution of 6.032 x 10^{-6}. Regression algorithms are also investigated for their potential to anticipate the sensor's performance without the need for manual simulations, which would save a lot of time and money. Therefore, the recommended sensor has increased the likelihood of properly recognizing a wide range of analytes, expanding the scope of various sensing techniques and offering innovative methods of analysis.

CHAPTER – 8

FABRICATION

8.1 Introduction:

The fabrication process of PCF SPR sensors involves the precise engineering of PCF structures to incorporate plasmonic elements, such as metallic coatings or nanoparticles, that facilitate the excitation and manipulation of surface plasmons. Target molecules can be detected with extreme sensitivity and precision thanks to the analysis of the analyte's response to the evanescent field made possible by these plasmonic components.

Over time, several fabrication methods, from conventional procedures to cutting-edge nanofabrication technologies, have been developed for PCF SPR sensors. The complex PCF structures with clearly defined features and geometries were produced using methods such as chemical vapor deposition (CVD), Stack and Draw method, Atomic Layer Deposition (ALD) etc. Some of the fabrication techniques are discussed below.

A number of factors, including material selection, PCF size, and plasmonic element usage, must be carefully taken into account during the design and production of PCF SPR sensors. The sensor's efficiency, sensitivity, and spatial resolution are all directly affected by these factors.

8.2 Chemical Vapor Deposition (CVD):

A versatile and widely used method for putting thin films and coatings onto substrates is chemical vapor deposition (CVD). It involves the controlled reaction of precursor gases to produce a chemical reaction and the deposition of a desired substance, usually at high temperatures [136]. The precursor gases are injected into the reaction chamber during CVD, where they conduct chemical reactions and generate volatile byproducts. The desired substance can now be deposited onto the substrate after the byproducts are taken out of the chamber. The ability to create high-quality films with exact control over thickness, content, and shape is one of the benefits of CVD. A variety of materials, including metals, semiconductors, ceramics, and polymers, can be used

using this scalable technique. CVD is used in many fields, including semiconductor production, optical coatings, and surface engineering, to create functional coatings with specialized qualities for uses like corrosion prevention, wear resistance, and the creation of electronic devices [137].
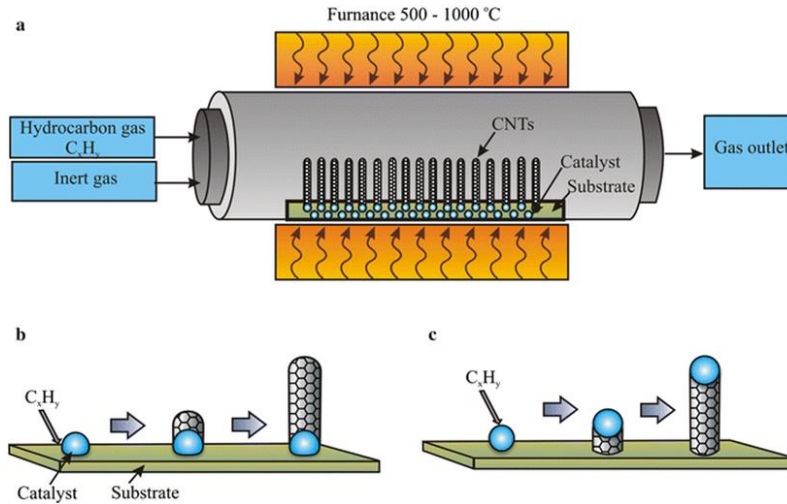
Figure 8.1: Chemical Vapor Deposition

8.3 Stack and Draw Method

A fabrication method utilized in the fabrication of PCF is stack and draw. It entails layering assembled rods in various configurations, each made of various substances with unique refractive indices and geometries. After being heated, these rods are fused together to create a solid structure [132].

In the manufacture of PCF, the stack and draw technique has various advantages. By choosing and ordering the various rod materials, it first allows the precise control of the PCF's geometry and refractive index profile. As a result, the optical features of the PCF, such as its mode confinement and dispersion characteristics, can be modified to match particular application needs.

Additionally, this technique enables the PCF structure to incorporate functional components. It is feasible to include dopants or nanoparticles that provide the PCF particular functionality, such as improved nonlinear optical properties or sensing capabilities, by carefully choosing the rod materials [138].

The stacked rods are heated and drawn into a long, thin fiber during the fabrication process. The preform is lengthened and its diameter is decreased throughout this drawing process, creating a highly regulated and consistent PCF structure. For the drawn fiber to have the appropriate final PCF configuration, additional post-processing procedures like splicing, coating, or tapering may be applied [139].

The stack and draw method offer a flexible and effective method for creating PCFs with specific functional components and optical qualities. Due to its adaptability and accuracy, it is a commonly utilized method in the manufacture of cutting-edge PCF-based devices for a variety of uses, including telecommunications, sensing, and high-power laser systems.
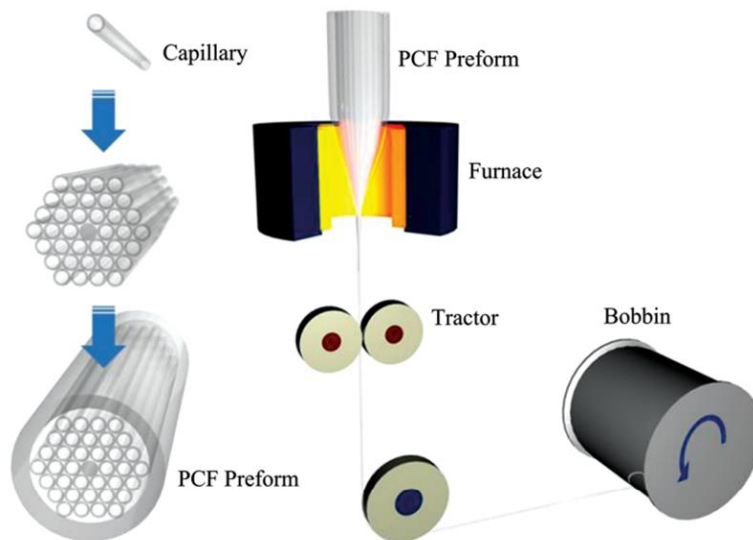
Figure 8.2: Stack and Draw method

8.4 Experimental Setup for the Sensor:

The experimental setup for the sensor, as illustrated in Figure 8.3, involves several components and procedures. Initially, a supercontinuum light source with a range of 450 nm to 1600 nm, such as the SuperK compact from NKTPhotonics™, is used to provide the incident light [140]. After passing via a polarizer and polarizer-controller, the light is then directed through the sensor using a single-mode fiber (SMF-28).

Following its passage through the sensor, the light is guided towards an Optical Spectrum Analyzer (specifically the AQ6370C model manufactured by Yokogawa™) utilizing a separate single-mode fiber [140]. The connection between the SMF-28 and the PCF sensor is established through splicing, which can be accomplished in two ways: either by inserting an etched SMF tip into the PCF or by employing the Vytran FFS-2000 splicer with filament fusion [141]. For this purpose, various high-efficiency SMF-PCF couplers can be utilized, offering a coupling efficiency range of 80-90%. Inside the sensor, a strategically positioned analyte channel allows for the introduction and removal of liquid analytes. The analyte is injected into the channel using a programmable micro injection pumper, specifically the LSP01-1A model manufactured by LongerPump™ [140], and the outlet of the channel is connected to a waste reservoir for storing the used analyte. When unknown analytes are present, they induce shifts in the resonance wavelength, which can be detected using the optical spectrum analyzer. These shifts in wavelength peaks are subsequently analyzed using a computer, which displays the final output spectra of the SPR measurements.
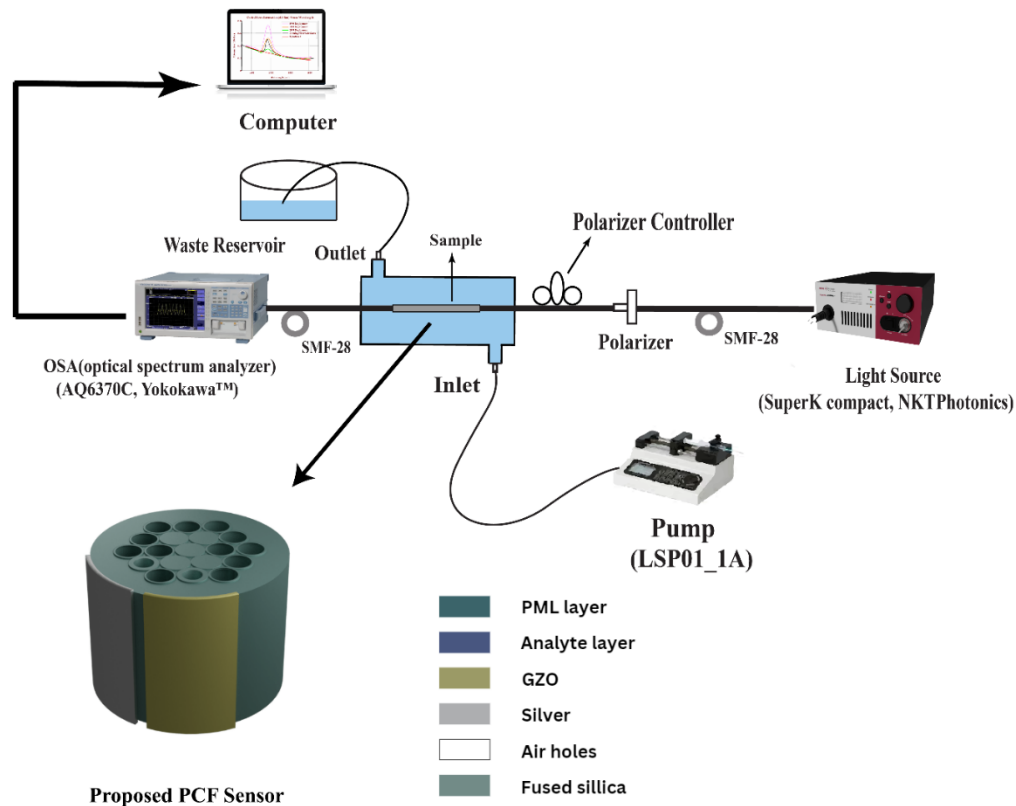
Figure 8.3: Experimental setup for our proposed sensor explained in chapter 7

CHAPTER – 9

FUTURE PROSPECTS AND CONCLUDING REMARKS

9.1 Future Work Scopes:

In our research work, we utilized Silver and GZO as plasmonic materials and incorporated circular air holes of varying diameters in our design. Silica was predominantly employed as the background material. We strongly believe that there are ample opportunities for further advancements in various applications of PCF sensors, along with continuous improvements in fiber performance such as:

- Exploring the potential of alternative plasmonic materials such as Graphene, AZO, ITO, etc., to enhance sensitivity and achieve improved results.
- Optimizing the sensor specifications with Deep Learning techniques or other optimization algorithms.
- Exploring different shapes of air holes other than circular, to further investigate the performance of the sensor.
- Improving the Amplitude Sensitivity and FOM of the sensor.
- Implementing multi-analyte channel-based sensors.
- Developing metal grating-based sensors.
- Magnetic field strength sensors and strain sensors can be approached.
- Enhancing the fabrication process to improve design and production efficiency.

9.2 Conclusion:

In this research, we utilized surface plasmon resonance (SPR) phenomenon to identify unknown analytes. By manipulating certain parameters of the PCF, we can control the evanescent field and tailor the propagation of light through the periodic air holes in the cladding region. Incorporating different plasmonic materials enhances sensor sensitivity. The maximum amplitude sensitivity (AS) and maximum wavelength sensitivity (WS) are key parameters that determine sensor effectiveness. The relatively newly developed parameter, DPSS, also needs to be extensively

researched. Throughout the thesis, we extensively discussed our sensor design, which contributes to detecting pharmaceutical products, biochemicals and medical procedures. This design features a perfectly matched layer (PML) surrounding the fiber to absorb the scattered evanescent field. We employed the full vectorial finite element method (FEM) in COMSOL Multiphysics simulation software to conduct numerical investigations and optimize fiber parameters for optimal sensing performance. Our sensor exhibits remarkable sensitivity values, low confinement loss and tolerance towards fabrication errors. It's simple yet strategic design facilitates practical fabrication using existing methods. Additionally, we explored the use of regression algorithms to predict sensor performance, enabling efficient and resource-saving evaluations. The use of ML algorithms can open new scope of research as the field is relatively newer and untouched. The proposed sensor holds great potential for advancements in sensing applications and medical diagnostics, owing to its feasible design and high sensitivity.

REFERENCES:

[1]   P. Englebienne, A. Van Hoonacker, and M. Verhas, "Surface plasmon resonance: principles, methods and applications in biomedical sciences," *Spectroscopy*, vol. 17, no. 2–3, pp. 255–273, 2003, doi: 10.1155/2003/372913.

[2]   S. Palomba and L. Novotny, "Nonlinear Excitation of Surface Plasmon Polaritons by Four-Wave Mixing," *Phys Rev Lett*, vol. 101, no. 5, p. 056802, Aug. 2008, doi: 10.1103/PhysRevLett.101.056802.

[3]   M. Kim, K. Park, E.-J. Jeong, Y.-B. Shin, and B. H. Chung, "Surface plasmon resonance imaging analysis of protein–protein interactions using on-chip-expressed capture protein," *Anal Biochem*, vol. 351, no. 2, pp. 298–304, Apr. 2006, doi: 10.1016/j.ab.2006.01.042.

[4]   S. Hearty, P. Leonard, H. Ma, and R. O'Kennedy, "Measuring Antibody-Antigen Binding Kinetics Using Surface Plasmon Resonance," 2018, pp. 421–455. doi: 10.1007/978-1-4939-8648-4_22.

[5]   Md. B. Hossain *et al.*, "Hybrid structure based high performance SPR sensor: a numerical approach of structure optimization for DNA hybridization," *Opt Quantum Electron*, vol. 53, no. 1, p. 24, Jan. 2021, doi: 10.1007/s11082-020-02650-9.

[6]   Md. S. Islam *et al.*, "A Novel Approach for Spectroscopic Chemical Identification Using Photonic Crystal Fiber in the Terahertz Regime," *IEEE Sens J*, vol. 18, no. 2, pp. 575–582, Jan. 2018, doi: 10.1109/JSEN.2017.2775642.

[7]   F. A. Mou, Md. M. Rahman, M. R. Islam, and M. I. H. Bhuiyan, "Development of a photonic crystal fiber for THz wave guidance and environmental pollutants detection," *Sens Biosensing Res*, vol. 29, p. 100346, Aug. 2020, doi: 10.1016/j.sbsr.2020.100346.

[8]   Md. M. Rahman, F. A. Mou, M. I. H. Bhuiyan, and M. R. Islam, "Photonic crystal fiber based terahertz sensor for cholesterol detection in human blood and liquid foodstuffs," *Sens Biosensing Res*, vol. 29, p. 100356, Aug. 2020, doi: 10.1016/j.sbsr.2020.100356.

[9]   Md. S. Islam *et al.*, "A novel Zeonex based photonic sensor for alcohol detection in beverages," in *2017 IEEE International Conference on Telecommunications and Photonics (ICTP)*, IEEE, Dec. 2017, pp. 114–118. doi: 10.1109/ICTP.2017.8285905.

[10]   Md. A. Islam, M. R. Islam, A. M. Al Naser, F. Anzum, and F. Z. Jaba, "Square structured photonic crystal fiber based THz sensor design for human body protein detection," *J Comput Electron*, vol. 20, no. 1, pp. 377–386, Feb. 2021, doi: 10.1007/s10825-020-01606-2.

[11]   M. R. Islam, A. N. M. Iftekher, F. A. Mou, Md. M. Rahman, and M. I. H. Bhuiyan, "Design of a Topas-based ultrahigh-sensitive PCF biosensor for blood component detection," *Applied Physics A*, vol. 127, no. 2, p. 109, Feb. 2021, doi: 10.1007/s00339-020-04261-3.

[12]   Md. A. Islam, M. R. Islam, S. Siraz, M. Rahman, M. S. Anzum, and F. Noor, "Wheel structured Zeonex-based photonic crystal fiber sensor in THz regime for sensing milk," *Applied Physics A*, vol. 127, no. 5, p. 311, May 2021, doi: 10.1007/s00339-021-04472-2.

[13]   M. R. Islam, A. N. M. Iftekher, F. Noor, M. R. H. Khan, Md. T. Reza, and M. M. Nishat, "AZO-coated plasmonic PCF nanosensor for blood constituent detection in near-infrared and visible spectrum," *Applied Physics A*, vol. 128, no. 1, p. 86, Jan. 2022, doi: 10.1007/s00339-021-05220-2.

[14]   Md. M. Rahman, F. A. Mou, M. I. H. Bhuiyan, and M. R. Islam, "Refractometric THz Sensing of Blood Components in a Photonic Crystal Fiber Platform," *Brazilian Journal of Physics*, vol. 52, no. 2, p. 47, Apr. 2022, doi: 10.1007/s13538-022-01054-2.

[15]   Md. M. Rahman, F. A. Mou, A. Al Mahmud, M. I. H. Bhuiyan, and M. R. Islam, "Photonic Crystal Fiber based Terahertz Sensor for Alcohol Detection in Beverages: Design and Analysis," in *2019 IEEE International Conference on Telecommunications and Photonics (ICTP)*, IEEE, Dec. 2019, pp. 1–4. doi: 10.1109/ICTP48844.2019.9041767.

[16]   M. R. Islam, M. Mamadou, and Md. S. Islam, "Design and analysis of a highly sensitive octagonal hollow core photonic crystal fiber for chemical sensing," *J Nanophotonics*, vol. 14, no. 03, Sep. 2020, doi: 10.1117/1.JNP.14.036014.

[17] M. Mitsushio, K. Miyashita, and M. Higo, "Sensor properties and surface characterization of the metal-deposited SPR optical fiber sensors with Au, Ag, Cu, and Al," *Sens Actuators A Phys*, vol. 125, no. 2, pp. 296–303, Jan. 2006, doi: 10.1016/j.sna.2005.08.019.

[18] M. R. Islam *et al.*, "Design of a quad channel SPR-based PCF sensor for analyte, strain, temperature, and magnetic field strength sensing," *Opt Quantum Electron*, vol. 54, no. 9, p. 563, Sep. 2022, doi: 10.1007/s11082-022-03912-4.

[19] M. R. Islam *et al.*, "Design of a hexagonal outlined porous cladding with vacant core photonic crystal fibre biosensor for cyanide detection at THz regime," *IET Optoelectronics*, vol. 16, no. 4, pp. 160–173, Aug. 2022, doi: 10.1049/ote2.12067.

[20] M. R. Islam *et al.*, "Trigonal cluster-based ultra-sensitive surface plasmon resonance sensor for multipurpose sensing," *Sens Biosensing Res*, vol. 35, p. 100477, Feb. 2022, doi: 10.1016/j.sbsr.2022.100477.

[21] Md. F. Hassan, R. H. Sagor, Md. R. Amin, M. R. Islam, and Md. S. Alam, "Point of Care Detection of Blood Electrolytes and Glucose Utilizing Nano-Dot Enhanced Plasmonic Biosensor," *IEEE Sens J*, vol. 21, no. 16, pp. 17749–17757, Aug. 2021, doi: 10.1109/JSEN.2021.3082756.

[22] M. R. Islam and M. Mamadou, "Spider web ultrasensitive terahertz photonic crystal fiber for chemical sensing," *Optical Engineering*, vol. 59, no. 08, Aug. 2020, doi: 10.1117/1.OE.59.8.087103.

[23] M. R. Islam *et al.*, "Design and analysis of birefringent SPR based PCF biosensor with ultra-high sensitivity and low loss," *Optik (Stuttg)*, vol. 221, p. 165311, Nov. 2020, doi: 10.1016/j.ijleo.2020.165311.

[24] M. Rakibul Islam, M. M. I. Khan, F. Mehjabin, J. Alam Chowdhury, and M. Islam, "Design of a fabrication friendly & highly sensitive surface plasmon resonance-based photonic crystal fiber biosensor," *Results Phys*, vol. 19, p. 103501, Dec. 2020, doi: 10.1016/j.rinp.2020.103501.

[25]   M. R. Islam *et al.*, "Surface plasmon resonance based highly sensitive gold coated PCF biosensor," *Applied Physics A*, vol. 127, no. 2, p. 118, Feb. 2021, doi: 10.1007/s00339-020-04162-5.

[26]   M. R. Islam *et al.*, "Design of a Dual Cluster and Dual Array-Based PCF-SPR Biosensor with Ultra-high WS and FOM," *Plasmonics*, vol. 17, no. 3, pp. 1171–1182, Jun. 2022, doi: 10.1007/s11468-022-01612-z.

[27]   M. R. Islam, E. Moazzam, R. L. Khan, R. Islam, and Z. Tasnim, "Analysis of a highly temperature-sensitive gold-coated plasmonic biosensor for analyte detection," *Ain Shams Engineering Journal*, vol. 14, no. 10, p. 102206, Oct. 2023, doi: 10.1016/j.asej.2023.102206.

[28]   M. R. Islam, E. Moazzam, R. Islam, R. L. Khan, and Z. Tasnim, "Design and Investigation of a low-loss Surface Plasmon resonance based PCF biosensor with a gold coated structure," in *2020 11th International Conference on Electrical and Computer Engineering (ICECE)*, IEEE, Dec. 2020, pp. 447–450. doi: 10.1109/ICECE51571.2020.9393045.

[29]   M. R. Islam, A. Hossain, Z. Mustafa, and T. Tahsin, "A Novel Photonic Crystal Fiber Biosensor Using Single Hexagonal Lattice Structure," in *2020 11th International Conference on Electrical and Computer Engineering (ICECE)*, IEEE, Dec. 2020, pp. 475–478. doi: 10.1109/ICECE51571.2020.9393151.

[30]   Md. S. Islam, S. Rana, M. R. Islam, M. Faisal, H. Rahman, and J. Sultana, "Porous core photonic crystal fibre for ultra-low material loss in THz regime," *IET Communications*, vol. 10, no. 16, pp. 2179–2183, Nov. 2016, doi: 10.1049/iet-com.2016.0227.

[31]   Md. S. Islam *et al.*, "Extremely low material loss and dispersion flattened TOPAS based circular porous fiber for long distance terahertz wave transmission," *Optical Fiber Technology*, vol. 34, pp. 6–11, Mar. 2017, doi: 10.1016/j.yofte.2016.11.014.

[32]   Md. M. Rahman, F. A. Mou, M. I. H. Bhuiyan, and M. R. Islam, "Extremely Low Effective Material Loss of Air Core Photonic Crystal Fiber for THz Guidance," in *2019*

IEEE Region 10 Symposium (TENSYMP), IEEE, Jun. 2019, pp. 716–720. doi: 10.1109/TENSYMP46218.2019.8971297.

[33]   M. R. Islam *et al.*, "An Eye-Shaped Ultra-Sensitive Localized Surface Plasmon Resonance–Based Biochemical Sensor," *Plasmonics*, vol. 17, no. 1, pp. 131–141, Feb. 2022, doi: 10.1007/s11468-021-01501-x.

[34]   M. R. Islam *et al.*, "Design of a dual spider-shaped surface plasmon resonance-based refractometric sensor with high amplitude sensitivity," *IET Optoelectronics*, vol. 17, no. 1, pp. 38–49, Feb. 2023, doi: 10.1049/ote2.12084.

[35]   Md. S. Islam *et al.*, "A modified hexagonal photonic crystal fiber for terahertz applications," *Opt Mater (Amst)*, vol. 79, pp. 336–339, May 2018, doi: 10.1016/j.optmat.2018.03.054.

[36]   A. Ramola, A. Marwaha, and S. Singh, "Design and investigation of a dedicated PCF SPR biosensor for CANCER exposure employing external sensing," *Applied Physics A*, vol. 127, no. 9, p. 643, Sep. 2021, doi: 10.1007/s00339-021-04785-2.

[37]   L. Li *et al.*, "Dual Kretschmann and Otto configuration fiber surface plasmon resonance biosensor," *Opt Express*, vol. 25, no. 22, p. 26950, Oct. 2017, doi: 10.1364/OE.25.026950.

[38]   R. Karlsson, "SPR for molecular interaction analysis: a review of emerging application areas," *Journal of Molecular Recognition*, vol. 17, no. 3, pp. 151–161, May 2004, doi: 10.1002/jmr.660.

[39]   F. Mumtaz *et al.*, "Numerical analysis of the highly non-linear and ultra-sensitive modified core of a photonic crystal fiber sensor for detection of liquid analytes," *Journal of the Optical Society of America B*, vol. 40, no. 1, p. 142, Jan. 2023, doi: 10.1364/JOSAB.478468.

[40]   M. R. H. Khan, F. A. M. Ali, and M. R. Islam, "THz sensing of CoViD-19 disinfecting products using photonic crystal fiber," *Sens Biosensing Res*, vol. 33, p. 100447, Aug. 2021, doi: 10.1016/j.sbsr.2021.100447.

[41] M. R. Islam *et al.*, "Design and numerical analysis of a gold-coated photonic crystal fiber based refractive index sensor," *Opt Quantum Electron*, vol. 53, no. 2, p. 112, Feb. 2021, doi: 10.1007/s11082-021-02748-8.

[42] S. I. Azzam, M. F. O. Hameed, R. E. A. Shehata, A. M. Heikal, and S. S. A. Obayya, "Multichannel photonic crystal fiber surface plasmon resonance based sensor," *Opt Quantum Electron*, vol. 48, no. 2, p. 142, Feb. 2016, doi: 10.1007/s11082-016-0414-4.

[43] T. Kundu, V. V. R. Sai, R. Dutta, S. Titas, P. Kumar, and S. Mukherjee, "Development of evanescent wave absorbance-based fibre-optic biosensor," *Pramana*, vol. 75, no. 6, pp. 1099–1113, Dec. 2010, doi: 10.1007/s12043-010-0193-6.

[44] M. R. Islam *et al.*, "Highly birefringent gold-coated SPR sensor with extremely enhanced amplitude and wavelength sensitivity," *The European Physical Journal Plus*, vol. 136, no. 2, p. 238, Feb. 2021, doi: 10.1140/epjp/s13360-021-01220-6.

[45] J. B. Maurya and Y. K. Prajapati, "A comparative study of different metal and prism in the surface plasmon resonance biosensor having MoS2-graphene," *Opt Quantum Electron*, vol. 48, no. 5, p. 280, May 2016, doi: 10.1007/s11082-016-0562-6.

[46] M. Rakibul Islam, A. N. M. Iftekher, K. Rakibul Hasan, Md. J. Nayen, and S. Bin Islam, "Dual-polarized highly sensitive surface-plasmon-resonance-based chemical and biomolecular sensor," *Appl Opt*, vol. 59, no. 11, p. 3296, Apr. 2020, doi: 10.1364/AO.383352.

[47] W. Gao *et al.*, "Experimental investigation on supercontinuum generation by single, dual, and triple wavelength pumping in a silica photonic crystal fiber," *Appl Opt*, vol. 55, no. 33, p. 9514, Nov. 2016, doi: 10.1364/AO.55.009514.

[48] A. Aming, M. Uthman, R. Chitaree, W. Mohammed, and B. M. A. Rahman, "Design and Characterization of Porous Core Polarization Maintaining Photonic Crystal Fiber for THz Guidance," *Journal of Lightwave Technology*, vol. 34, no. 23, pp. 5583–5590, Dec. 2016, doi: 10.1109/JLT.2016.2623657.

[49] N. Muduli and H. K. Padhy, "An optimized configuration of large mode field area PMMA photonic crystal fiber with low bending loss: a new approach," *Journal of Materials*

Science: Materials in Electronics, vol. 27, no. 2, pp. 1906–1912, Feb. 2016, doi: 10.1007/s10854-015-3972-5.

[50]   Md. Sohidul Islam, Jamilur Rahman, and Mohammad Rakibul Islam, "Topas Based Low Loss and Dispersion Flatten Decagonal Porous Core Photonic Crystal Fiber for Terahertz Communication," *INTERNATIONAL JOURNAL OF MICROWAVE AND OPTICAL TECHNOLOG*, vol. 14, no. 1, pp. 62–69, Jan. 2019.

[51]   Md. S. Islam, K. M. Samaun Reza, and M. Rakibul Islam, "Low loss topas based porous core single mode photonic crystal fiber for THz communications," *Indian Journal of Pure & Applied Physics (IJPAP)*, vol. 57, no. 11, pp. 836–841, 2019.

[52]   Md. S. Islam *et al.*, "Extremely low material loss and dispersion flattened TOPAS based circular porous fiber for long distance terahertz wave transmission," *Optical Fiber Technology*, vol. 34, pp. 6–11, Mar. 2017, doi: 10.1016/j.yofte.2016.11.014.

[53]   M. S. Islam, K. M. Samaun Reza, and M. R. Islam, "Topas based high birefringent and low loss single mode hybrid-core porous fiber for broadband application.," *Indian Journal of Pure & Applied Physics (IJPAP)*, vol. 56, no. (5), pp. 399–404, 2018.

[54]   Md. S. Islam *et al.*, "Zeonex-based asymmetrical terahertz photonic crystal fiber for multichannel communication and polarization maintaining applications," *Appl Opt*, vol. 57, no. 4, p. 666, Feb. 2018, doi: 10.1364/AO.57.000666.

[55]   Md. S. Islam *et al.*, "Zeonex-based asymmetrical terahertz photonic crystal fiber for multichannel communication and polarization maintaining applications," *Appl Opt*, vol. 57, no. 4, p. 666, Feb. 2018, doi: 10.1364/AO.57.000666.

[56]   Md. A. Islam, M. R. Islam, S. Siraz, M. Rahman, M. S. Anzum, and F. Noor, "Wheel structured Zeonex-based photonic crystal fiber sensor in THz regime for sensing milk," *Applied Physics A*, vol. 127, no. 5, p. 311, May 2021, doi: 10.1007/s00339-021-04472-2.

[57]   J. Sultana, M. R. Islam, M. Faisal, K. Md. Abu Talha, and Md. S. Islam, "Design and analysis of a Zeonex based diamond-shaped core kagome lattice photonic crystal fiber for T-ray wave transmission," *Optical Fiber Technology*, vol. 47, pp. 55–60, Jan. 2019, doi: 10.1016/j.yofte.2018.11.017.

[58] H. Han, H. Park, M. Cho, and J. Kim, "Terahertz pulse propagation in a plastic photonic crystal fiber," *Appl Phys Lett*, vol. 80, no. 15, pp. 2634–2636, Apr. 2002, doi: 10.1063/1.1468897.

[59] Md. Moshiur Rahman, F. Akter Mou, M. Imamul Hassan Bhuiyan, and M. Rakibul Islam, "Design and characterization of a circular sectored core cladding structured photonic crystal fiber with ultra-low EML and flattened dispersion in the THz regime," *Optical Fiber Technology*, vol. 55, p. 102158, Mar. 2020, doi: 10.1016/j.yofte.2020.102158.

[60] K. KANESHIMA, "Numerical Investigation of Octagonal Photonic Crystal Fibers with Strong Confinement Field," *IEICE Transactions on Electronics*, vol. E89-C, no. 6, pp. 830–837, Jun. 2006, doi: 10.1093/ietele/e89-c.6.830.

[61] S. Rana, R. Islam, Md. S. Islam, and M. R. Islam, "Low loss rotated porous core octagonal single-mode fiber for THz radiation," in *2016 5th International Conference on Informatics, Electronics and Vision (ICIEV)*, IEEE, May 2016, pp. 166–169. doi: 10.1109/ICIEV.2016.7759989.

[62] Md. A. Islam, M. R. Islam, Z. Tasnim, R. Islam, R. L. Khan, and E. Moazzam, "Low-Loss and Dispersion-Flattened Octagonal Porous Core PCF for Terahertz Transmission Applications," *Iranian Journal of Science and Technology, Transactions of Electrical Engineering*, vol. 44, no. 4, pp. 1583–1592, Dec. 2020, doi: 10.1007/s40998-020-00337-1.

[63] S. Li, "Equiangular spiral photonic crystal fiber for code synchronization in all-optical analog-to-digital conversion based on lumped time delay compensation scheme," *Optik (Stuttg)*, vol. 127, no. 11, pp. 4693–4697, Jun. 2016, doi: 10.1016/j.ijleo.2016.02.017.

[64] Md. S. Islam, J. Sultana, J. Atai, D. Abbott, S. Rana, and M. R. Islam, "Ultra low-loss hybrid core porous fiber for broadband applications," *Appl Opt*, vol. 56, no. 4, p. 1232, Feb. 2017, doi: 10.1364/AO.56.001232.

[65] Md. S. Islam *et al.*, "Low loss and low dispersion hybrid core photonic crystal fiber for terahertz propagation," *Photonic Network Communications*, vol. 35, no. 3, pp. 364–373, Jun. 2018, doi: 10.1007/s11107-017-0751-7.

[66] M. R. Islam *et al.*, "Design and Analysis of a Biochemical Sensor Based on Surface Plasmon Resonance with Ultra-high Sensitivity," *Plasmonics*, vol. 16, no. 3, pp. 849–861, Jun. 2021, doi: 10.1007/s11468-020-01355-9.

[67] M. R. Islam, A. N. M. Iftekher, I. Marshad, N. F. Rity, and R. U. Ahmad, "Analysis of a dual peak dual plasmonic layered LSPR-PCF sensor – Double peak shift sensitivity approach," *Optik (Stuttg)*, vol. 280, p. 170793, Jun. 2023, doi: 10.1016/j.ijleo.2023.170793.

[68] A. A. Rifat, G. A. Mahdiraji, Y. G. Shee, Md. J. Shawon, and F. R. M. Adikan, "A Novel Photonic Crystal Fiber Biosensor Using Surface Plasmon Resonance," *Procedia Eng*, vol. 140, pp. 1–7, 2016, doi: 10.1016/j.proeng.2015.08.1107.

[69] C. Liu *et al.*, "Numerical analysis of a photonic crystal fiber based on a surface plasmon resonance sensor with an annular analyte channel," *Opt Commun*, vol. 382, pp. 162–166, Jan. 2017, doi: 10.1016/j.optcom.2016.07.031.

[70] F. Wang, Z. Sun, C. Liu, T. Sun, and P. K. Chu, "A Highly Sensitive Dual-Core Photonic Crystal Fiber Based on a Surface Plasmon Resonance Biosensor with Silver-Graphene Layer," *Plasmonics*, vol. 12, no. 6, pp. 1847–1853, Dec. 2017, doi: 10.1007/s11468-016-0453-5.

[71] A. A. Rifat *et al.*, "Photonic crystal fiber based plasmonic sensors," *Sens Actuators B Chem*, vol. 243, pp. 311–325, May 2017, doi: 10.1016/j.snb.2016.11.113.

[72] X. Yu *et al.*, "A selectively coated photonic crystal fiber based surface plasmon resonance sensor," *Journal of Optics*, vol. 12, no. 1, p. 015005, Jan. 2010, doi: 10.1088/2040-8978/12/1/015005.

[73] M. R. Islam, A. N. M. Iftekher, F. A. Mou, Md. M. Rahman, and M. I. H. Bhuiyan, "Design of a Topas-based ultrahigh-sensitive PCF biosensor for blood component detection," *Applied Physics A*, vol. 127, no. 2, p. 109, Feb. 2021, doi: 10.1007/s00339-020-04261-3.

[74]   J. Sultana *et al.*, "Highly birefringent elliptical core photonic crystal fiber for terahertz application," *Opt Commun*, vol. 407, pp. 92–96, Jan. 2018, doi: 10.1016/j.optcom.2017.09.020.

[75]   S. Islam *et al.*, "Extremely low-loss, dispersion flattened porous-core photonic crystal fiber for terahertz regime," *Optical Engineering*, vol. 55, no. 7, p. 076117, Jul. 2016, doi: 10.1117/1.OE.55.7.076117.

[76]   M. R. Islam, Md. F. Kabir, K. Md. A. Talha, and Md. S. Islam, "A novel hollow core terahertz refractometric sensor," *Sens Biosensing Res*, vol. 25, p. 100295, Sep. 2019, doi: 10.1016/j.sbsr.2019.100295.

[77]   M. R. Islam, Md. F. Kabir, K. Md. A. Talha, and Md. S. Arefin, "Highly birefringent honeycomb cladding terahertz fiber for polarization-maintaining applications," *Optical Engineering*, vol. 59, no. 01, p. 1, Jan. 2020, doi: 10.1117/1.OE.59.1.016113.

[78]   M. R. Islam, Md. A. Hossain, K. Md. A. Talha, and R. K. Munia, "A novel hollow core photonic sensor for liquid analyte detection in the terahertz spectrum: design and analysis," *Opt Quantum Electron*, vol. 52, no. 9, p. 415, Sep. 2020, doi: 10.1007/s11082-020-02532-0.

[79]   F. A. Mou, Md. M. Rahman, Md. A. Al Mahmud, M. R. Islam, and M. I. H. Bhuiyan, "Design and Characterization of a Low Loss Polarization Maintaining Photonic Crystal Fiber for THz Regime," in *2019 IEEE International Conference on Telecommunications and Photonics (ICTP)*, IEEE, Dec. 2019, pp. 1–4. doi: 10.1109/ICTP48844.2019.9041715.

[80]   S. Rana *et al.*, "A highly birefringent slotted-core THz fiber," in *2016 9th International Conference on Electrical and Computer Engineering (ICECE)*, IEEE, Dec. 2016, pp. 226–229. doi: 10.1109/ICECE.2016.7853897.

[81]   M. R. Islam, F. A. Mou, Md. M. Rahman, and M. I. Hassan Bhuiyan, "Hollow core photonic crystal fiber for chemicals sensing in liquid analytes: Design and analysis," *Int J Mod Phys B*, vol. 34, no. 28, p. 2050259, Nov. 2020, doi: 10.1142/S0217979220502598.

[82]   M. R. Islam, Md. Arif Hossain, S. I. Ali, J. Sultana, and Md. Saiful Islam, "Design and Characterization of an Ultra Low Loss, Dispersion-Flattened Slotted Photonic Crystal

Fiber for Terahertz Application," *Journal of Optical Communications*, vol. 42, no. 4, pp. 619–626, Oct. 2021, doi: 10.1515/joc-2018-0152.

[83] M. R. H. Khan, A. A. Chowdhury, M. R. Islam, M. S. Hosen, M. H. Mim, and M. M. Nishat, "Wave-Shaped Microstructure Cancer Detection Sensor in Terahertz Band: Design and Analysis," *Applied Sciences*, vol. 13, no. 9, p. 5784, May 2023, doi: 10.3390/app13095784.

[84] Md. A. Al Mahmud, M. R. Islam, A. N. M. Iftekher, Md. M. Rahman, and F. A. Mou, "Design and numerical analysis of a porous core photonic crystal fiber for refractometric THz sensing," *Microsystem Technologies*, vol. 29, no. 1, pp. 115–126, Jan. 2023, doi: 10.1007/s00542-022-05396-4.

[85] J. Hammond, N. Bhalla, S. Rafiee, and P. Estrela, "Localized Surface Plasmon Resonance as a Biosensing Platform for Developing Countries," *Biosensors (Basel)*, vol. 4, no. 2, pp. 172–188, Jun. 2014, doi: 10.3390/bios4020172.

[86] D. Paul and R. Biswas, "Highly sensitive LSPR based photonic crystal fiber sensor with embodiment of nanospheres in different material domain," *Opt Laser Technol*, vol. 101, pp. 379–387, May 2018, doi: 10.1016/j.optlastec.2017.11.040.

[87] Md. A. Mollah and Md. S. Islam, "Novel Single Hole Exposed-Suspended Core Localized Surface Plasmon Resonance Sensor," *IEEE Sens J*, pp. 1–1, 2020, doi: 10.1109/JSEN.2020.3023975.

[88] B. Liedberg, C. Nylander, and I. Lunström, "Surface plasmon resonance for gas detection and biosensing," *Sensors and Actuators*, vol. 4, pp. 299–304, Jan. 1983, doi: 10.1016/0250-6874(83)85036-7.

[89] M. Hautakorpi, M. Mattinen, and H. Ludvigsen, "Surface-plasmon-resonance sensor based on three-hole microstructured optical fiber," *Opt Express*, vol. 16, no. 12, p. 8427, Jun. 2008, doi: 10.1364/OE.16.008427.

[90] A. Hassani and M. Skorobogatiy, "Design criteria for microstructured-optical-fiber-based surface-plasmon-resonance sensors," *Journal of the Optical Society of America B*, vol. 24, no. 6, p. 1423, Jun. 2007, doi: 10.1364/JOSAB.24.001423.

[91]   B. Shuai, L. Xia, and D. Liu, "Coexistence of positive and negative refractive index sensitivity in the liquid-core photonic crystal fiber based plasmonic sensor," *Opt Express*, vol. 20, no. 23, p. 25858, Nov. 2012, doi: 10.1364/OE.20.025858.

[92]   J. Wu, S. Li, X. Wang, M. Shi, X. Feng, and Y. Liu, "Ultrahigh sensitivity refractive index sensor of a D-shaped PCF based on surface plasmon resonance," *Appl Opt*, vol. 57, no. 15, p. 4002, May 2018, doi: 10.1364/AO.57.004002.

[93]   Md. E. Rahaman, R. Saha, Md. S. Ahsan, and I.-B. Sohn, "Design and Performance Analysis of a D–shaped PCF and Surface Plasmon Resonance Based Glucose Sensor," in *2018 4th International Conference on Electrical Engineering and Information & Communication Technology (iCEEiCT)*, IEEE, Sep. 2018, pp. 325–329. doi: 10.1109/CEEICT.2018.8628080.

[94]   E. Haque, Md. A. Hossain, F. Ahmed, and Y. Namihira, "Surface Plasmon Resonance Sensor Based on Modified <![CDATA[<inline-formula> <tex-math notation="LaTeX">D </tex-math> </inline-formula>]]>-Shaped Photonic Crystal Fiber for Wider Range of Refractive Index Detection," *IEEE Sens J*, vol. 18, no. 20, pp. 8287–8293, Oct. 2018, doi: 10.1109/JSEN.2018.2865514.

[95]   Md. A. Khalek, S. Chakma, B. K. Paul, and K. Ahmed, "Dataset of surface plasmon resonance based on photonic crystal fiber for chemical sensing applications," *Data Brief*, vol. 19, pp. 76–81, Aug. 2018, doi: 10.1016/j.dib.2018.05.026.

[96]   Q. M. Kamrunnahar, J. R. Mou, and M. Momtaj, "Dual-core gold coated photonic crystal fiber plasmonic sensor: Design and analysis," *Results Phys*, vol. 18, p. 103319, Sep. 2020, doi: 10.1016/j.rinp.2020.103319.

[97]   S. M. Abu Sufian Sunny, T. Ahmed, A. Anzum, and A. K. Paul, "Performance Analysis of a PCF SPR Based Highly Sensitive Biosensor," in *2019 IEEE International Conference on Biomedical Engineering, Computer and Information Technology for Health (BECITHCON)*, IEEE, Nov. 2019, pp. 7–10. doi: 10.1109/BECITHCON48839.2019.9063192.

[98] Md. Mahabubur Rahman, Md. Aslam Molla, A. Kumar Paul, Md. A. Based, Md. Masud Rana, and M. S. Anower, "Numerical investigation of a highly sensitive plasmonic refractive index sensor utilizing hexagonal lattice of photonic crystal fiber," *Results Phys*, vol. 18, p. 103313, Sep. 2020, doi: 10.1016/j.rinp.2020.103313.

[99] Md. N. Hossen, Md. Ferdous, Md. Abdul Khalek, S. Chakma, B. K. Paul, and K. Ahmed, "Design and analysis of biosensor based on surface plasmon resonance," *Sens Biosensing Res*, vol. 21, pp. 1–6, Nov. 2018, doi: 10.1016/j.sbsr.2018.08.003.

[100] Md. R. Hasan *et al.*, "Spiral Photonic Crystal Fiber-Based Dual-Polarized Surface Plasmon Resonance Biosensor," *IEEE Sens J*, vol. 18, no. 1, pp. 133–140, Jan. 2018, doi: 10.1109/JSEN.2017.2769720.

[101] S. Chu, K. Nakkeeran, A. M. Abobaker, S. S. Aphale, P. R. Babu, and K. Senthilnathan, "Design and Analysis of Surface-Plasmon-Resonance-Based Photonic Quasi-Crystal Fiber Biosensor for High-Refractive-Index Liquid Analytes," *IEEE Journal of Selected Topics in Quantum Electronics*, vol. 25, no. 2, pp. 1–9, Mar. 2019, doi: 10.1109/JSTQE.2018.2873481.

[102] P. R. West, S. Ishii, G. V. Naik, N. K. Emani, V. M. Shalaev, and A. Boltasseva, "Searching for better plasmonic materials," *Laser Photon Rev*, vol. 4, no. 6, pp. 795–808, Nov. 2010, doi: 10.1002/lpor.200900055.

[103] A. A. Rifat *et al.*, "Surface Plasmon Resonance Photonic Crystal Fiber Biosensor: A Practical Sensing Approach," *IEEE Photonics Technology Letters*, vol. 27, no. 15, pp. 1628–1631, Aug. 2015, doi: 10.1109/LPT.2015.2432812.

[104] S. Szunerits, V. G. Praig, M. Manesse, and R. Boukherroub, "Gold island films on indium tin oxide for localized surface plasmon sensing," *Nanotechnology*, vol. 19, no. 19, p. 195712, May 2008, doi: 10.1088/0957-4484/19/19/195712.

[105] M. Kanso, S. Cuenot, and G. Louarn, "Roughness effect on the SPR measurements for an optical fibre configuration: experimental and numerical approaches," *Journal of Optics A: Pure and Applied Optics*, vol. 9, no. 7, pp. 586–592, Jul. 2007, doi: 10.1088/1464-4258/9/7/008.

[106] P. B. Johnson and R. W. Christy, "Optical Constants of the Noble Metals," *Phys Rev B*, vol. 6, no. 12, pp. 4370–4379, Dec. 1972, doi: 10.1103/PhysRevB.6.4370.

[107] J. Han *et al.*, "Asymmetrical photonic crystal fiber based on the surface plasmon resonance sensor and analysis by the lower-birefringence peak method," *Optik (Stuttg)*, vol. 189, pp. 121–129, Jul. 2019, doi: 10.1016/j.ijleo.2019.05.070.

[108] M. R. Momota and Md. R. Hasan, "Hollow-core silver coated photonic crystal fiber plasmonic sensor," *Opt Mater (Amst)*, vol. 76, pp. 287–294, Feb. 2018, doi: 10.1016/j.optmat.2017.12.049.

[109] D. Kumar, M. Sharma, and V. Singh, "Surface Plasmon resonance implemented silver thin film PCF sensor with multiple – Hole microstructure for wide ranged refractive index detection," *Mater Today Proc*, vol. 62, pp. 6590–6595, 2022, doi: 10.1016/j.matpr.2022.04.598.

[110] J. N. Dash, R. Das, and R. Jha, "AZO Coated Microchannel Incorporated PCF-Based SPR Sensor: A Numerical Analysis," *IEEE Photonics Technology Letters*, vol. 30, no. 11, pp. 1032–1035, Jun. 2018, doi: 10.1109/LPT.2018.2829920.

[111] K. M. M. Rahman and S. Rahman, "Ultra-Wide Refractive Index Range Photonic Crystal Fiber Based Sensor with Gallium Doped Zinc Oxide Coating," in *2021 5th International Conference on Electrical Engineering and Information Communication Technology (ICEEICT)*, IEEE, Nov. 2021, pp. 1–6. doi: 10.1109/ICEEICT53905.2021.9667813.

[112] T. Li, L. Zhu, X. Yang, X. Lou, and L. Yu, "A Refractive Index Sensor Based on H-Shaped Photonic Crystal Fibers Coated with Ag-Graphene Layers," *Sensors*, vol. 20, no. 3, p. 741, Jan. 2020, doi: 10.3390/s20030741.

[113] J. N. Dash and R. Jha, "On the Performance of Graphene-Based D-Shaped Photonic Crystal Fibre Biosensor Using Surface Plasmon Resonance," *Plasmonics*, vol. 10, no. 5, pp. 1123–1131, Oct. 2015, doi: 10.1007/s11468-015-9912-7.

[114] V. Kaur and S. Singh, "Design of D-Shaped PCF-SPR sensor with dual coating of ITO and ZnO conducting metal oxide," *Optik (Stuttg)*, vol. 220, p. 165135, Oct. 2020, doi: 10.1016/j.ijleo.2020.165135.

[115] M. Rakibul Islam, A. N. M. Iftekher, M. S. Anzum, M. Rahman, and S. Siraz, "LSPR Based Double Peak Double Plasmonic Layered Bent Core PCF-SPR Sensor for Ultra-Broadband Dual Peak Sensing," *IEEE Sens J*, vol. 22, no. 6, pp. 5628–5635, Mar. 2022, doi: 10.1109/JSEN.2022.3149715.

[116] M. R. Islam, A. N. M. Iftekher, M. F. Etu, W. R. Rashmi, and S. Abbas, "Dual Peak Double Resonance Sensing Using a Dual Plasmonic Material PCF-SPR Sensor," *Plasmonics*, vol. 18, no. 3, pp. 983–993, Jun. 2023, doi: 10.1007/s11468-023-01829-6.

[117] S. Selvendran, J. Divya, A. Sivanantha Raja, A. Sivasubramanian, and S. Itapu, "A Reconfigurable Surface-Plasmon-Based Filter/Sensor Using D-Shaped Photonic Crystal Fiber," *Micromachines (Basel)*, vol. 13, no. 6, p. 917, Jun. 2022, doi: 10.3390/mi13060917.

[118] G. V. Naik, V. M. Shalaev, and A. Boltasseva, "Alternative Plasmonic Materials: Beyond Gold and Silver," *Advanced Materials*, vol. 25, no. 24, pp. 3264–3294, Jun. 2013, doi: 10.1002/adma.201205076.

[119] https://www.rp-photonics.com/silica_fibers.html, "RP Photonics Encyclopedia - silica fibers, optical fiber, glass, fiber optics."

[120] B. K. Paul *et al.*, "The design and analysis of a dual-diamond-ring PCF-based sensor," *J Comput Electron*, vol. 19, no. 3, pp. 1288–1294, Sep. 2020, doi: 10.1007/s10825-020-01509-2.

[121] Md. S. Islam *et al.*, "A Hi-Bi Ultra-Sensitive Surface Plasmon Resonance Fiber Sensor," *IEEE Access*, vol. 7, pp. 79085–79094, 2019, doi: 10.1109/ACCESS.2019.2922663.

[122] F. Haider, R. A. Aoni, R. Ahmed, Md. S. Islam, and A. E. Miroshnichenko, "Propagation Controlled Photonic Crystal Fiber-Based Plasmonic Sensor <italic>via</italic> Scaled-Down Approach," *IEEE Sens J*, vol. 19, no. 3, pp. 962–969, Feb. 2019, doi: 10.1109/JSEN.2018.2880161.

[123] S. Chakma, M. A. Khalek, B. K. Paul, K. Ahmed, M. R. Hasan, and A. N. Bahar, "Gold-coated photonic crystal fiber biosensor based on surface plasmon resonance: Design and

analysis," *Sens Biosensing Res*, vol. 18, pp. 7–12, Apr. 2018, doi: 10.1016/j.sbsr.2018.02.003.

[124] Md. S. Islam *et al.*, "Dual-polarized highly sensitive plasmonic sensor in the visible to near-IR spectrum," *Opt Express*, vol. 26, no. 23, p. 30347, Nov. 2018, doi: 10.1364/OE.26.030347.

[125] S. Hassan *et al.*, "Comparative Analysis of Machine Learning Algorithms in Detection of Brain Tumor," in *2022 3rd International Conference on Big Data Analytics and Practices (IBDAP)*, IEEE, Sep. 2022, pp. 31–36. doi: 10.1109/IBDAP55587.2022.9907433.

[126] D. Maulud and A. M. Abdulazeez, "A Review on Linear Regression Comprehensive in Machine Learning," *Journal of Applied Science and Technology Trends*, vol. 1, no. 4, pp. 140–147, Dec. 2020, doi: 10.38094/jastt1457.

[127] M. F. O. Hameed, S. S. A. Obayya, K. Al-Begain, A. M. Nasr, and M. I. Abo el Maaty, "Accurate radial basis function based neural network approach for analysis of photonic crystal fibers," *Opt Quantum Electron*, vol. 40, no. 11–12, pp. 891–905, Sep. 2008, doi: 10.1007/s11082-009-9290-5.

[128] S. Chugh, A. Gulistan, S. Ghosh, and B. M. A. Rahman, "Machine learning approach for computing optical properties of a photonic crystal fiber," *Opt Express*, vol. 27, no. 25, p. 36414, Dec. 2019, doi: 10.1364/OE.27.036414.

[129] G. Fornarelli, L. Mescia, F. Prudenzano, M. De Sario, and F. Vacca, "A neural network model of erbium-doped photonic crystal fibre amplifiers," *Opt Laser Technol*, vol. 41, no. 5, pp. 580–585, Jul. 2009, doi: 10.1016/j.optlastec.2008.10.010.

[130] I. Abdelaziz, F. AbdelMalek, S. Haxha, H. Ademgil, and H. Bouchriha, "Photonic Crystal Fiber With an Ultrahigh Birefringence and Flattened Dispersion by Using Genetic Algorithms," *Journal of Lightwave Technology*, vol. 31, no. 2, pp. 343–348, Jan. 2013, doi: 10.1109/JLT.2012.2226866.

[131] X. Yang, Y. Lu, B. Liu, and J. Yao, "Analysis of Graphene-Based Photonic Crystal Fiber Sensor Using Birefringence and Surface Plasmon Resonance," *Plasmonics*, vol. 12, no. 2, pp. 489–496, Apr. 2017, doi: 10.1007/s11468-016-0289-z.

[132] G. Amouzad Mahdiraji *et al.*, "Challenges and Solutions in Fabrication of Silica-Based Photonic Crystal Fibers: An Experimental Study," *Fiber and Integrated Optics*, vol. 33, no. 1–2, pp. 85–104, Jan. 2014, doi: 10.1080/01468030.2013.879680.

[133] R. F. Cregan *et al.*, "Single-Mode Photonic Band Gap Guidance of Light in Air," *Science (1979)*, vol. 285, no. 5433, pp. 1537–1539, Sep. 1999, doi: 10.1126/science.285.5433.1537.

[134] S. Choi and J.-K. Park, "Two-step photolithography to fabricate multilevel microchannels," *Biomicrofluidics*, vol. 4, no. 4, p. 046503, Dec. 2010, doi: 10.1063/1.3517230.

[135] P. Ho, "Chemical Vapor Deposition for Microelectronics: Principles, Technology and ApplicationsArthur Sherman (Noyes Publications, 1987)," *MRS Bull*, vol. 13, no. 11, pp. 78–78, Nov. 1988, doi: 10.1557/S0883769400064046.

[136] M. Hadi, A. Rouhollahi, and M. Yousefi, "Nanocrystalline graphite-like pyrolytic carbon film electrode for electrochemical sensing of hydrazine," *Sens Actuators B Chem*, vol. 160, no. 1, pp. 121–128, Dec. 2011, doi: 10.1016/j.snb.2011.07.022.

[137] J. Batey and E. Tierney, "Low-temperature deposition of high-quality silicon dioxide by plasma-enhanced chemical vapor deposition," *J Appl Phys*, vol. 60, no. 9, pp. 3136–3145, Nov. 1986, doi: 10.1063/1.337726.

[138] V. V. Velmiskin, O. N. Egorova, V. Mishkin, K. Nishchev, and S. L. Semjonov, "Active material for fiber core made by powder-in-tube method: subsequent homogenization by means of stack-and-draw technique," K. Kalli and A. Mendez, Eds., Jun. 2012, p. 84260I. doi: 10.1117/12.922188.

[139] L. R. Murphy, S. Yerolatsitis, T. A. Birks, and J. M. Stone, "Stack, seal, evacuate, draw: a method for drawing hollow-core fiber stacks under positive and negative pressure," *Opt Express*, vol. 30, no. 21, p. 37303, Oct. 2022, doi: 10.1364/OE.470599.

[140] Z. Liu *et al.*, "Reflective-distributed SPR sensor based on twin-core fiber," *Opt Commun*, vol. 366, pp. 107–111, May 2016, doi: 10.1016/j.optcom.2015.12.018.

[141] M. Murawski, L. R. Jaroszewicz, and K. Stasiewicz, "A photonic crystal fiber splice with a standard single mode fiber," *Photonics Lett Pol*, vol. 1, no. 3, Sep. 2009, doi: 10.4302/plp.2009.3.05.